
Projected GANs Converge Faster

Axel Sauer^{1,2} Kashyap Chitta^{1,2} Jens Müller³ Andreas Geiger^{1,2}
¹University of Tübingen ²Max Planck Institute for Intelligent Systems, Tübingen
³Computer Vision and Learning Lab, University Heidelberg
²{firstname.lastname}@tue.mpg.de ³{firstname.lastname}@iwr.uni-heidelberg.de

Abstract

Generative Adversarial Networks (GANs) produce high-quality images but are challenging to train. They need careful regularization, vast amounts of compute, and expensive hyper-parameter sweeps. We make significant headway on these issues by projecting generated and real samples into a fixed, pretrained feature space. Motivated by the finding that the discriminator cannot fully exploit features from deeper layers of the pretrained model, we propose a more effective strategy that mixes features across channels and resolutions. Our Projected GAN improves image quality, sample efficiency, and convergence speed. It is further compatible with resolutions of up to one Megapixel and advances the state-of-the-art Fréchet Inception Distance (FID) on twenty-two benchmark datasets. Importantly, Projected GANs match the previously lowest FIDs up to 40 times faster, cutting the wall-clock time from 5 days to less than 3 hours given the same computational resources.



Figure 1: **Convergence with Projected GANs.** Evolution of samples for a fixed latent code during training on the AFHQ-Dog dataset [7]. We find that discriminating features in the projected feature space speeds up convergence and yields lower FIDs. This finding is consistent across many datasets.

1 Introduction

A Generative Adversarial Network (GAN) consists of a generator and a discriminator. For image synthesis, the generator’s task is to generate an RGB image; the discriminator aims to distinguish real from fake samples. On closer inspection, the discriminator’s task is two-fold: First, it projects the real and fake samples into a meaningful space, i.e., it learns a representation of the input space. Second, it discriminates based on this representation. Unfortunately, training the discriminator jointly with the generator is a notoriously hard task. While discriminator regularization techniques help to balance the adversarial game [43], standard regularization methods like gradient penalties [50] are susceptible to hyperparameter choices [33] and can lead to a substantial decrease in performance [5].

In this paper, we explore the utility of pretrained representations to improve and stabilize GAN training. Using pretrained representations has become ubiquitous in computer vision [40, 41, 62]

and natural language processing [24, 59, 61]. While combining pretrained perceptual networks [73] with GANs for image-to-image translation has led to impressive results [19, 63, 75, 81], this idea has not yet materialized for unconditional noise-to-image synthesis. Indeed, we confirm that a naïve application of this idea does not lead to state-of-the-art results (Section 4) as strong pretrained features enable the discriminator to dominate the two-player game, resulting in vanishing gradients for the generator [2]. In this work, we demonstrate how these challenges can be overcome and identify two key components for exploiting the full potential of pretrained perceptual feature spaces for GAN training: **feature pyramids** to enable multi-scale feedback with multiple discriminators and **random projections** to better utilize deeper layers of the pretrained network.

We conduct extensive experiments on small and large datasets with a resolution of up to 1024^2 pixels. Across all datasets, we demonstrate state-of-the-art image synthesis results at significantly reduced training time (Fig. 1). We also find that Projected GANs increase data efficiency and avoid the need for additional regularization, rendering expensive hyperparameter sweeps unnecessary. Code, models, and supplementary videos can be found on the project page <https://sites.google.com/view/projected-gan>.

2 Related Work

We categorize related work into two main areas: pretraining for GANs and discriminator design.

Pretrained Models for GAN Training. Work on leveraging pretrained representations for GANs can be divided into two categories: First, transferring parts of a GAN to a new dataset [21, 52, 82, 88] and, second, using pretrained models to control and improve GANs. The latter is advantageous as pretraining does not need to be adversarial. Our work falls into this second category. Pretrained models can be used as a guiding mechanism to disentangle causal generative factors [69], for text-driven image manipulation [58], matching the generator activations to inverted classifiers [25, 71], or to generate images via gradient ascent in the latent space of a generator [55]. The non-adversarial approach of [68] learns generative models with moment matching in pretrained models; however, the results remain far from competitive to standard GANs. An established method is the combination of adversarial and perceptual losses [28]. Commonly, the losses are combined additively [15, 19, 45, 67, 81]. Additive combination, however, is only possible if a reconstruction target is available, e.g., in paired image-to-image translation settings [92]. Instead of providing the pretrained network with a reconstruction target, Sungatullina et al. [75] propose to optimize an adversarial loss on frozen VGG features [73]. They show that their approach improves CycleGAN [92] on image translation tasks. In a similar vein, [63] recently proposed a different perceptual discriminator. They utilize a pretrained VGG and connect its features with the prediction of a pretrained segmentation network. The combined features are fed into multiple discriminators at different scales. The two last approaches are specific to the image-to-image translation task. We demonstrate that these methods do not work well for the more challenging unconditional setting where the entire image content is synthesized from a random latent code.

Discriminator Design. Much work on GANs focuses on novel generator architectures [5, 33, 34, 86], while the discriminator often remains close to a vanilla convolutional neural network or mirrors the generator. Notable exceptions are [70, 87] which utilize an encoder-decoder discriminator architecture. However, in contrast to us, they neither use pretrained features nor random projections. A different line of work considers a setup with multiple discriminators, applied to either the generated RGB image [13, 18] or low-dimensional projections thereof [1, 54]. The use of several discriminators promises improved sample diversity, training speed, and training stability. However, these approaches are not utilized in current state-of-the-art systems because of diminishing returns compared to the increased computational effort. Providing multi-scale feedback with one or multiple discriminators has been helpful for both image synthesis [30, 31] and image-to-image translation [57, 81]. While these works interpolate the RGB image at different resolutions, our findings indicate the importance of multi-scale *feature maps*, showing parallels to the success of pyramid networks for object detection [48]. Lastly, to prevent overfitting of the discriminator, differentiable augmentation methods have recently been proposed [32, 79, 89, 90]. We find that adopting these strategies helps exploit the full potential of pretrained representations for GAN training.

3 Projected GANs

GANs aim to model the distribution of a given training dataset. A generator G maps latent vectors \mathbf{z} sampled from a simple distribution $\mathbb{P}_{\mathbf{z}}$ (typically a normal distribution) to corresponding generated samples $G(\mathbf{z})$. The discriminator D then aims to distinguish real samples $\mathbf{x} \sim \mathbb{P}_{\mathbf{x}}$ from the generated samples $G(\mathbf{z}) \sim \mathbb{P}_{G(\mathbf{z})}$. This basic idea results in the following minimax objective

$$\min_G \max_D \left(\mathbb{E}_{\mathbf{x}}[\log D(\mathbf{x})] + \mathbb{E}_{\mathbf{z}}[\log(1 - D(G(\mathbf{z})))] \right) \quad (1)$$

We introduce a set of feature projectors $\{P_l\}$ which map real and generated images to the discriminator’s input space. Projected GAN training can thus be formulated as follows

$$\min_G \max_{\{D_l\}} \sum_{l \in \mathcal{L}} \left(\mathbb{E}_{\mathbf{x}}[\log D_l(P_l(\mathbf{x}))] + \mathbb{E}_{\mathbf{z}}[\log(1 - D_l(P_l(G(\mathbf{z}))))] \right) \quad (2)$$

where $\{D_l\}$ is a set of independent discriminators operating on different feature projections. Note that we keep $\{P_l\}$ fixed in (3) and only optimize the parameters of G and $\{D_l\}$. The feature projectors $\{P_l\}$ should satisfy two necessary conditions: they should be differentiable and provide sufficient statistics of their inputs, i.e., they should preserve important information. Moreover, we aim to find feature projectors $\{P_l\}$ which turn the (difficult to optimize) objective in (1) into an objective more amenable to gradient-based optimization. We now show that a projected GAN indeed matches the distribution in the projected feature space, before specifying the details of our feature projectors.

3.1 Consistency

The projected GAN objective in (3) no longer optimizes directly to match the true distribution \mathbb{P}_T . To understand the training properties under ideal conditions, we consider a more generalized form of the consistency theorem of [54]:

Theorem 1. *Let \mathbb{P}_T denote the density of the true data distribution and \mathbb{P}_G the density of the distribution the Generator G produces. Let $P_l \circ T$ and $P_l \circ G$ be the functional composition of the differentiable and fixed function P_l and the true/generated data distribution, and \mathbf{y} be the transformed input to the discriminator. For a fixed G , the optimal discriminators are given by*

$$D_{l,G}^*(\mathbf{y}) = \frac{\mathbb{P}_{P_l \circ T}(\mathbf{y})}{\mathbb{P}_{P_l \circ T}(\mathbf{y}) + \mathbb{P}_{P_l \circ G}(\mathbf{y})}$$

for all $l \in \mathcal{L}$. In this case, the optimal G under (3) is achieved iff $\mathbb{P}_{P_l \circ T} = \mathbb{P}_{P_l \circ G}$ for all $l \in \mathcal{L}$.

A proof of the theorem is provided in the appendix. From the theorem, we conclude that a feature projector P_l with its associated discriminator D_l encourages the generator to match the true distribution along the marginal through P_l . Therefore, at convergence, G matches the generated and true distributions in feature space. The theorem also holds when using stochastic data augmentations [32] before the deterministic projections P_l .

3.2 Model Overview

Projecting to and training in pretrained feature spaces opens up a realm of new questions which we address below. This section will provide an overview of the general system and is followed by extensive ablations of each design choice. As our feature projections affect the discriminator, we focus on P_l and D_l in this section and postpone the discussion of generator architectures to Section 5.

Multi-Scale Discriminators. We obtain features from four layers L_l of a pretrained feature network F at resolutions ($L_1 = 64^2, L_2 = 32^2, L_3 = 16^2, L_4 = 8^2$). We associate a separate discriminator D_l with the features at layer L_l , respectively. Each discriminator D_l uses a simple convolutional architecture with spectral normalization [51] at each convolutional layer. We observe better performance if all discriminators output logits at the same resolution (4^2). Accordingly, we use fewer down-sampling blocks for lower resolution inputs. Following common practice, we sum all logits for computing the overall loss. For the generator pass, we sum the losses of all discriminators. More complex strategies [1, 18] did not improve performance in our experiments.

Random Projections. We observe that features at deeper layers are significantly harder to cover, as evidenced by our experiments in Section 4. We hypothesize that a discriminator can focus on a subset of the feature space while wholly disregarding other parts. This problem might be especially

prominent in the deeper, more semantic layers. Therefore, we propose two different strategies to dilute prominent features, encouraging the discriminator to utilize all available information equally. Common to both strategies is that they mix features using differentiable random projections which are fixed, i.e., after random initialization, the parameters of these layers are not trained.

Cross-Channel Mixing (CCM). Empirically, we found two properties to be desirable: (i) the random projection should be information preserving to leverage the full representational power of F , and (ii) it should not be trivially invertible. The easiest way to mix across channels is a 1×1 convolution. A 1×1 convolution with an equal number of output and input channels is a generalization of a permutation [38] and consequently preserves information about its input. In practice, we find that more output channels lead to better performance as the mapping remains injective and therefore information preserving. Kingma et al. [38] initialize their convolutional layers as a random rotation matrix as a good starting point for optimization. We do not find this to improve GAN performance (see Appendix), arguably since it violates (ii). We therefore randomly initialize the weights of the convolutional layer via Kaiming initialization [22]. Note that we do not add any activation functions. We apply this random projection at each of the four scales and feed the transformed feature to the discriminator as depicted in Fig. 2.

Cross-Scale Mixing (CSM). To encourage feature mixing *across* scales, CSM extends CCM with random 3×3 convolutions and bilinear upsampling, yielding a U-Net [65] architecture, see Fig. 3. However, our CSM block is simpler than a vanilla U-Net [65]: we only use a single convolutional layer at each scale. As for CCM, we utilize Kaiming initialization for all weights.

Pretrained Feature Networks. We ablate over varying feature networks. First, we investigate different versions of EfficientNets, which allow for direct control over model size versus performance. EfficientNets are image classification models trained on ImageNet [10] and designed to provide favorable accuracy-compute tradeoffs. Second, we use ResNets of varying sizes. To analyze the dependency on ImageNet features (Section 4.3), we also consider R50-CLIP [60], a ResNet optimized with a contrastive language-image objective on a dataset of 400 million (image, text) pairs. Lastly, we utilize a vision transformer architecture (ViT-Base) [14] and its efficient follow-up (DeiT-small distilled) [78]. We do not choose an inception network [76] to avoid strong correlations with the evaluation metric FID [23]. In the appendix, we also evaluate several other neural and non-neural metrics to rule out correlations. These additional metrics reflect the rankings obtained by FID.

In the following, we conduct a systematic ablation study to analyze the importance and best configuration of each component in our Projected GAN model, before comparing it to the state-of-the-art.

4 Ablation Study

To determine the best configuration of discriminators, mixing strategy, and pretrained feature network, we conduct experiments on LSUN-Church [84], which is medium-sized (126k images) and reasonably visually complex, using a resolution of 256^2 pixels. For the generator G we use the generator architecture of FastGAN [49], consisting of several upsampling blocks, with additional skip-layer-excitation blocks. Using a hinge loss [47], we train with a batch size of 64 until 1 million real images have been shown to the discriminator, a sufficient amount for G to reach values close to convergence. If not specified otherwise, we use an EfficientNet-Lite1 [77] feature network in this section. We found that discriminator augmentation [32, 79, 89, 90] consistently improves the performance of all methods, and is required to reach state-of-the-art performance. We leverage differentiable data-augmentation [89] which we found to yield the best results in combination with the FastGAN generator.

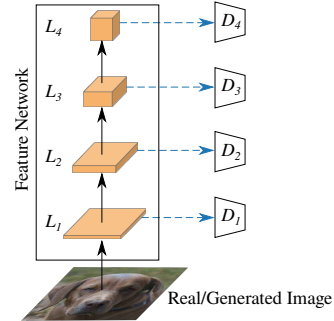


Figure 2: **CCM** (dashed blue arrows) employs 1×1 convolutions with random weights.

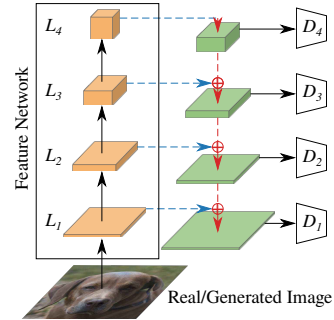


Figure 3: **CSM** (dashed red arrows) adds random 3×3 convolutions and bilinear upsampling, yielding a U-Net.

Discriminator(s)	$rel-FD_1 \downarrow$	$rel-FD_2 \downarrow$	$rel-FD_3 \downarrow$	$rel-FD_4 \downarrow$	$rel - FID \downarrow$
No Projection					
on L_1	0.56	0.32	0.31	0.55	0.66
on L_1, L_2	0.35	0.21	0.23	0.47	0.53
on L_1, L_2, L_3	0.42	0.26	0.28	0.64	0.90
on L_1, L_2, L_3, L_4	0.46	0.34	0.38	0.79	1.15
on L_2, L_3, L_4	0.95	0.67	0.71	1.19	1.99
on L_3, L_4	2.14	1.41	1.18	1.99	3.46
on L_4	10.92	5.74	2.56	2.79	5.08
Perceptual D	2.98	1.76	1.20	1.89	2.73
CCM					
on L_1	0.27	0.21	0.26	0.50	0.59
on L_1, L_2	0.27	0.18	0.21	0.41	0.48
on L_1, L_2, L_3	0.31	0.25	0.24	0.54	0.67
on L_1, L_2, L_3, L_4	0.53	0.34	0.34	0.59	0.77
Perceptual D	5.33	3.06	2.14	1.09	4.77
CCM + CSM					
on L_1	0.34	0.25	0.19	0.35	0.44
on L_1, L_2	0.21	0.18	0.16	0.27	0.31
on L_1, L_2, L_3	0.41	0.26	0.17	0.23	0.29
on L_1, L_2, L_3, L_4	0.26	0.16	0.13	0.16	0.24
Perceptual D	2.53	1.37	0.89	0.43	2.13

Table 1: **Feature Space Fréchet Distances.** We aim to find the best combination of discriminators and random projections to fit the distributions in feature network F . We show the relative FD at different layers of F ($rel-FD_i$) between 50k generated and real images on LSUN-Church. $rel-FD_i$ is **normalized** using the baseline Fréchet Distances for a model with a standard single RGB image discriminator. Hence, values > 1 indicate worse performance than the RGB baseline. We report $rel-FD$ for four layers of an EfficientNet (L_1, L_2, L_3 and L_4 from shallow to deep), as well as relative Fréchet Inception Distance (FID) [23]. Note that $rel-FD_i$ should not be compared between different feature spaces, i.e., only within-column comparisons are meaningful. Blue boxes highlight the layers which we supervise via independent discriminators. The green box corresponds to a perceptual discriminator [75], which takes in all feature maps at once.

4.1 Which feature network layers are most informative?

We first investigate the relevance of independent multi-scale discriminators. For this experiment, we do not use feature mixing. To measure how well G fits a particular feature space, we employ the Fréchet Distance (FD) [17] on the spatially pooled features denoted as FD_i for layer i . FDs across different feature spaces are not directly comparable. Therefore, we train a GAN baseline with a standard RGB discriminator, record FD_i^{RGB} at each layer and quantify the relative improvement via the fraction $rel-FD_i = FD_i / FD_i^{RGB}$. We also investigate a perceptual discriminator [75], where feature maps are fed into different layers of the *same* discriminator to predict a single logit.

The results in Table 1 (No Projection) show that two discriminators are better than one and improve over the vanilla RGB baseline. Surprisingly, adding discriminators at deep layers hurts performance. We conclude that these more semantic features do not respond well to direct adversarial losses. We also experimented with discriminators at resized versions of the original image, but could not find a setting of hyperparameters and architectures that improves over the single image baseline. Omitting the discriminators on the shallow features decreases performance, which is anticipated, as these layers contain most of the information about the original image. A similar effect has been observed for feature inversion [16] – the deeper the layer, the harder it is to reconstruct its input. Lastly, we observe that independent discriminators outperform the perceptual discriminator by a significant margin.

	EfficientNet					ResNet			Transformer	
	lite0	lite1	lite2	lite3	lite4	R18	R50	R50-CLIP	DeiT	ViT
Params (M) ↓	2.96	3.72	4.36	6.42	11.15	11.18	23.51	23.53	92.36	317.52
IN top-1 ↑	75.48	76.64	77.47	79.82	81.54	69.75	79.04	N/A	85.42	85.16
FID ↓	2.53	1.65	1.69	1.79	2.35	4.16	4.40	3.80	2.46	12.38

Table 2: **Pretrained Feature Networks Study.** We train the projected GAN with different pretrained feature networks. We find that compact EfficientNets outperform both ResNets and Transformers.

4.2 How can we best utilize the pretrained features?

Given the insights from the previous section, we aim to improve the utilization of deep features. For this experiment, we only investigate configurations that include discriminators at high resolutions. Table 1 (CCM and CCM + CSM) presents the results for both mixing strategies. CCM moderately decreases the FDs across all settings, confirming our hypothesis that mixing channels results in better feedback for the generator. When adding CSM, we achieve another notable improvement across all configurations. Especially $rel-FD_i$ at deeper layers are significantly decreased, demonstrating CSM’s usefulness to leverage deep semantic features. Interestingly, we observe that the best performance is now obtained by combining all four discriminators. A perceptual discriminator is again inferior to multiple discriminators. We remark that integrating the original image, via an independent discriminator or CCM or CSM always resulted in worse performance. This failure suggests that naively combining non-projected with projected adversarial optimization impairs training dynamics.

4.3 Which feature network architecture is most effective?

Using the best setting determined by the experiments above (CCM + CSM with four discriminators), we study the effectiveness of various perceptual feature network architectures for Projected GAN training. To ensure convergence, also for larger architectures, we train for 10 million images. Table 2 reports the FIDs achieved on LSUN-Church. Surprisingly, we find that there is no correlation with ImageNet accuracy. On the contrary, we observe lower FIDs for smaller models (e.g., EfficientNets-lite). This observation indicates that a more *compact* representation is beneficial while at the same time reducing computational overhead and consequently training time. R50-CLIP slightly outperforms its R50 counterpart, indicating that ImageNet features are not required to achieve low FID. For the sake of completeness, we also train with randomly initialized feature networks, which, however, converge to much higher FID values (see Appendix). In the following, we thus use EfficientNet-Lite1 as our feature network.

5 Comparison to State-of-the-Art

This section conducts a comprehensive analysis demonstrating the advantages of Projected GANs with respect to state-of-the-art models. Our experiments are structured into three sections: evaluation of convergence speed and data efficiency (5.1), and comparisons on large (5.2) and small (5.3) benchmark datasets. We cover a wide variety of datasets in terms of size (hundreds to millions of samples), resolution (256^2 to 1024^2), and visual complexity (clip-art, paintings, and photographs).

Evaluation Protocol. We measure image quality using the Fréchet Inception Distance (FID) [23]. Following [33, 34], we report the FID between 50k generated and all real images. We select the snapshot with the best FID for each method. In addition to image quality, we include a metric to evaluate convergence. As in [32], we measure training progress based on the number of real images shown to the discriminator (*_imgs*). We report the number of images required by the model for the FID to reach values within 5% of the best FID over training. In the appendix, we also report other metrics that are less benchmarked in GAN literature: KID [4], SwAV-FID [53], precision and recall [66]. Unless otherwise specified, we follow the evaluation protocol of [26] to facilitate fair comparisons. Specifically, we compare all approaches given the same fixed number of images (10 million). With this setting, each experiment takes roughly 100-200 GPU hours on a NVIDIA V100, for more details we refer to the appendix.

Baselines. We use StyleGAN2-ADA [32] and FastGAN [49] as baselines. StyleGAN2-ADA is the strongest model on most datasets in terms of sample quality, whereas FastGAN excels in training speed. We implement these baselines and our Projected GANs within the codebase provided by the authors of StyleGAN2-ADA [32]. For each model, we ran two kinds of data augmentation:

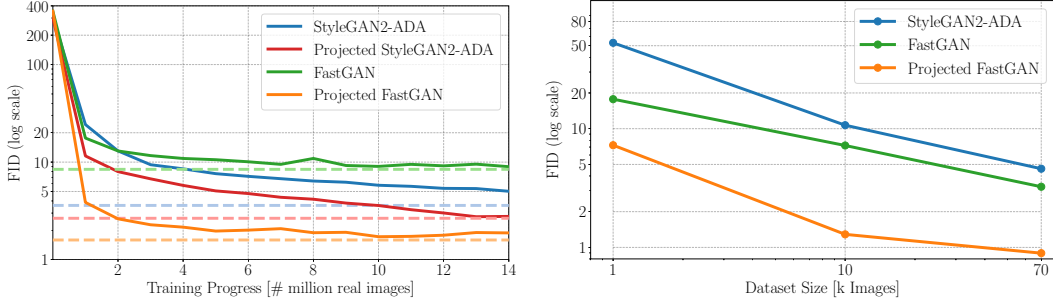


Figure 4: **Training Properties.** Left: Projected FastGAN surpasses the best FID of StyleGAN2 (at 88 M images) after just 1.1 M images on LSUN-Church. Right: Projected FastGAN yields significantly improved FID scores, even when using subsets of CLEVR with 1k and 10k samples.



Figure 5: **Training progress on LSUN church at 256² pixels.** Shown are samples for a fixed noise vector \mathbf{z} over k images. From top to bottom: FastGAN, StyleGAN2-ADA, Projected GAN.

differentiable data-augmentation [89] and adaptive discriminator augmentation [32]. We select the better performing augmentation strategy per model. For all baselines and datasets, we perform data amplification through x-flips. Projected GANs use the same generator and discriminator architecture and training hyperparameters (learning rate and batch size) for all experiments. For high-resolution image generation, additional upsampling blocks are included in the generator to match the desired output resolution. We carefully tune all hyper-parameters for both baselines for best results: we find that FastGAN is sensitive to the choice of batch size, and StyleGAN2-ADA to the learning rate and R1 penalty. The appendix documents additional implementation details used in each of our experiments.

5.1 Convergence Speed and Data Efficiency

Following [26] and [85], we analyze the training properties of Projected GANs on LSUN-Church at an image resolution of 256² pixels and on the 70k CLEVR dataset [29]. In this section, we also train longer than 10 M images if necessary, as we are interested in convergence properties.

Convergence Speed. We apply projected GAN training for both the style-based generator of StyleGAN2 and the standard generator with a single input noise vector of FastGAN. As shown in Fig. 4 (left), FastGAN converges quickly but saturates at a high FID. StyleGAN2 converges more slowly (88 M images) but reaches a lower FID. Projected GAN training improves both generators. Particularly for FastGAN, improvements in both convergence speed and final FID are significant while improvements for StyleGAN2 are less pronounced. Remarkably, *Projected FastGAN* reaches the previously best FID of StyleGAN2 after experiencing only 1.1 M images as compared to 88 M of StyleGAN2. In wall clock time, this corresponds to less than 3 hours instead of 5 days. Hence, from now on, we utilize the FastGAN generator and refer to this model simply as *Projected GAN*.

Fig. 5 shows samples for a fixed noise vector \mathbf{z} during training on LSUN-Church. For both FastGAN and StyleGAN, patches of texture gradually morph into a global structure. For Projected GAN, we directly observe the emergence of structure which becomes more detailed over time. Interestingly, the Projected GAN latent space appears to be very volatile, i.e., for fixed \mathbf{z} the images undergo significant perceptual changes during training. In the non-projected cases, these changes are more gradual. We hypothesize that this induced volatility might be due to the discriminator providing more *semantic* feedback compared to conventional RGB losses. Such semantic feedback could introduce

more stochasticity during training which in turn improves convergence and performance. We also observed that the signed real logits of the discriminator remain at the same level throughout training (see Appendix). Stable signed logits indicate that the discriminator does not suffer from overfitting.

Sample Efficiency. The use of pretrained models is generally linked to improved sample efficiency. To evaluate this property, we also created two subsets of the 70k CLEVR dataset by randomly sub-sampling 10k and 1k images from it, respectively. As depicted in Fig. 4 (right), our Projected GAN significantly improves over both baselines across all dataset splits.

5.2 Large Datasets

Besides CLEVR and LSUN-Church, we benchmark Projected GANs against various state-of-the-art models on three other large datasets: LSUN-Bedroom [84] (3M indoor bedroom scenes), FFHQ [33] (70k images of faces) and Cityscapes [9] (25k driving scenes captured from a vehicle). For all datasets, we use an image resolution of 256^2 pixels. As Cityscapes and CLEVR images are not of aspect ratio 1:1 we resize them to 256^2 for training. Besides StyleGAN2-ADA and FastGAN, we compare against SAGAN [86] and GANsformers [26]. All models were trained for 10 M images. For the large datasets, we also report numbers for StyleGAN2 trained for more than 10 M images to report the lowest FID values achieved in previous literature (denoted as StyleGAN2*). In the appendix, we report results on nine more large datasets.

Table 3 shows that the Projected GAN outperforms all state-of-the-art models in terms of FID values on all datasets by a large margin. For example, on LSUN-Bedroom, it achieves an FID value of 1.52 compared to 6.15 by GANsformer, the previously best model in this setting. Projected GAN achieves state-of-the-art FID values remarkably fast, e.g., on LSUN-church, it achieves an FID value of 3.18 after 1.1 M *_imgs*. StyleGAN2 has obtained the previously lowest FID value of 3.39 after 88 M *_imgs*, 80 times as many as needed by Projected GAN. Similar speed-ups are also realized for all other large datasets as shown in Table 3. Interestingly, when training longer on FFHQ (39 M *_imgs*), we observe further improvements of Projected GAN to an FID of 2.2. Note that all five datasets represent very different objects in various scenes. This demonstrates that the performance gain is robust to the choice of the dataset, although the feature network is trained only on ImageNet. It is important to note that the main improvements are based on improved sample diversity as indicated by recall which we report in the appendix. The improvement in diversity is most notable on large datasets, e.g., LSUN church, where the image fidelity appears to be similar to StyleGAN.

5.3 Small Datasets

To further evaluate our method in the few-shot setting, we compare against StyleGAN2-ADA and FastGAN on art paintings from WikiArt (1000 images; wikiart.org), Oxford Flowers (1360 images) [56], photographs of landscapes (4319 images; flickr.com), AnimalFace-Dog (389 images) [72] and Pokemon (833 images; pokemon.com). Further, we report results on high-resolution versions of Pokemon and Art-Painting (1024^2). Lastly, we evaluate on AFHQ-Cat, -Dog and -Wild at 512^2 [7]. The AFHQ datasets contain $\sim 5k$ closeups per category cat, dog, or wildlife. We do not have a license to re-distribute these datasets, but we provide the URLs to enable reproducibility, similar to [49].

Projected GAN outperforms all baselines in terms of FID values by a significant margin on all datasets and all resolutions as shown in Table 3. Remarkably, our model beats the prior state-of-the-art on all datasets (256^2) after observing fewer than 600k images. For AnimalFace-Dog, the Projected GAN surpasses the previously best FID after only 20k images. One might argue that the EfficientNet used as feature network facilitates data generation for the animal datasets as EfficientNet is trained on ImageNet which contains many animal classes (e.g., 120 classes for dog breeds). However, it is interesting to observe that Projected GANs also achieve state-of-the-art FID on Pokemon and Art Painting though these datasets differ significantly from ImageNet. This evidences the generality of ImageNet features. For the high-resolution datasets, Projected GANs achieve the same FID value many times faster than the best baselines, e.g., ten times faster than StyleGAN2-ADA on AFHQ-Cat or four times faster than FastGAN on Pokemon. We remark that F and D_l generalize to any resolution as they are fully convolutional.

6 Discussion and Future Work

While we achieve low FID on all datasets, we also identify two systematic failure cases: As depicted in Fig. 7, we sometimes observe “floating heads” on AFHQ. In a few samples, the animals appear in high quality but resemble cutouts on blurry or bland backgrounds. We hypothesize that generating a realistic background and image composition is less critical when a prominent object is already depicted. This hypothesis follows from the fact that we used image classification models for the projection, which have been shown to only marginally reduce in accuracy when applied on images of objects with removed background [83]. On FFHQ, projected GAN sometimes produces poor-quality samples with wrong proportions and artifacts, even at state-of-the-art FID, see Fig. 8.



Figure 7: "Floating Heads"



Figure 8: Artifacts on FFHQ.

In terms of generators, StyleGAN is more challenging to tune and does not profit as much from projected training. The FastGAN generator is fast to optimize but simultaneously produced unrealistic samples in some parts of the latent space – a problem that could be solved by a mapping network similar to StyleGAN. Hence, we speculate that unifying the strengths of both architectures in combination with projected training might improve performance further. Moreover, our study of different pretrained networks indicates that efficient models are especially suitable for projected GAN training. Exploring this connection in-depth, and in general, determining desirable feature space properties opens up exciting new research opportunities. Lastly, our work advances efficiency for generative models. More efficient models lower the barrier of computational effort needed for generating realistic images. A lower barrier facilitates malignant use of generative models (e.g., “deep fakes”) while simultaneously also democratizing research in this area.

Acknowledgments and Disclosure of Funding

We acknowledge the financial support by the BMWi in the project KI Delta Learning (project number 19A190130). Andreas Geiger was supported by the ERC Starting Grant LEGO-3D (850533). Kashyap Chitta was supported by the German Federal Ministry of Education and Research (BMBF): Tübingen AI Center, FKZ: 01IS18039B and the International Max Planck Research School for Intelligent Systems (IMPRS-IS). Jens Müller received funding by the Heidelberg Collaboratory for Image Processing (HCI). We thank the Center for Information Services and High Performance Computing (ZIH) at Dresden University of Technology for generous allocations of computation time. Lastly, we would like to thank Vanessa Sauer for her general support.

References

- [1] I. Albuquerque, J. Monteiro, T. Doan, B. Considine, T. Falk, and I. Mitliagkas. Multi-objective training of generative adversarial networks with multiple discriminators. In *Proc. of the International Conf. on Machine learning (ICML)*, 2019. 2, 3
- [2] M. Arjovsky and L. Bottou. Towards principled methods for training generative adversarial networks. In *Proc. of the International Conf. on Learning Representations (ICLR)*, 2017. 2
- [3] S. Azadi, M. Tschannen, E. Tzeng, S. Gelly, T. Darrell, and M. Lucic. Semantic bottleneck scene generation. *arXiv.org*, 2019. 17
- [4] M. Binkowski, D. J. Sutherland, M. Arbel, and A. Gretton. Demystifying MMD gans. In *Proc. of the International Conf. on Learning Representations (ICLR)*, 2018. 6, 16
- [5] A. Brock, J. Donahue, and K. Simonyan. Large scale GAN training for high fidelity natural image synthesis. In *Proc. of the International Conf. on Learning Representations (ICLR)*, 2019. 1, 2
- [6] M. Caron, I. Misra, J. Mairal, P. Goyal, P. Bojanowski, and A. Joulin. Unsupervised learning of visual features by contrasting cluster assignments. *arXiv.org*, 2006.09882, 2020. 16, 30
- [7] Y. Choi, Y. Uh, J. Yoo, and J.-W. Ha. Stargan v2: Diverse image synthesis for multiple domains. In *Proc. IEEE Conf. on Computer Vision and Pattern Recognition (CVPR)*, 2020. 1, 8

- [8] A. Coates, A. Ng, and H. Lee. An analysis of single-layer networks in unsupervised feature learning. In *Proc. of the Conf. on Artificial Intelligence (AAAI)*, 2011. 17
- [9] M. Cordts, M. Omran, S. Ramos, T. Rehfeld, M. Enzweiler, R. Benenson, U. Franke, S. Roth, and B. Schiele. The cityscapes dataset for semantic urban scene understanding. In *Proc. IEEE Conf. on Computer Vision and Pattern Recognition (CVPR)*, 2016. 8
- [10] J. Deng, W. Dong, R. Socher, L. jia Li, K. Li, and L. Fei-fei. Imagenet: A large-scale hierarchical image database. In *Proc. IEEE Conf. on Computer Vision and Pattern Recognition (CVPR)*, 2009. 4
- [11] K. Desai and J. Johnson. Virtex: Learning visual representations from textual annotations. In *Proc. IEEE Conf. on Computer Vision and Pattern Recognition (CVPR)*, 2021. 16
- [12] P. Dhariwal and A. Nichol. Diffusion models beat gans on image synthesis. *arXiv.org*, 2021. 21
- [13] T. Doan, J. Monteiro, I. Albuquerque, B. Mazoure, A. Durand, J. Pineau, and R. D. Hjelm. On-line adaptative curriculum learning for gans. In *Proc. of the Conf. on Artificial Intelligence (AAAI)*, 2019. 2
- [14] A. Dosovitskiy, L. Beyer, A. Kolesnikov, D. Weissenborn, X. Zhai, T. Unterthiner, M. Dehghani, M. Minderer, G. Heigold, S. Gelly, J. Uszkoreit, and N. Houlsby. An image is worth 16x16 words: Transformers for image recognition at scale. In *Proc. of the International Conf. on Learning Representations (ICLR)*, 2021. 4
- [15] A. Dosovitskiy and T. Brox. Generating images with perceptual similarity metrics based on deep networks. In *Advances in Neural Information Processing Systems (NIPS)*, 2016. 2
- [16] A. Dosovitskiy and T. Brox. Inverting visual representations with convolutional networks. In *Proc. IEEE Conf. on Computer Vision and Pattern Recognition (CVPR)*, 2016. 5
- [17] D. Dowson and B. Landau. The fréchet distance between multivariate normal distributions. *Journal of multivariate analysis*, 1982. 5
- [18] I. Durugkar, I. Gemp, and S. Mahadevan. Generative multi-adversarial networks. In *Proc. of the International Conf. on Learning Representations (ICLR)*, 2017. 2, 3
- [19] P. Esser, R. Rombach, and B. Ommer. Taming transformers for high-resolution image synthesis. In *Proc. IEEE Conf. on Computer Vision and Pattern Recognition (CVPR)*, 2020. 2
- [20] I. J. Goodfellow, J. Pouget-Abadie, M. Mirza, B. Xu, D. Warde-Farley, S. Ozair, A. C. Courville, and Y. Bengio. Generative adversarial nets. In *Advances in Neural Information Processing Systems (NIPS)*, 2014. 15
- [21] H. Ham, T. J. Jun, and D. Kim. Unbalanced gans: Pre-training the generator of generative adversarial network using variational autoencoder. *arXiv.org*, 2002.02112, 2020. 2
- [22] K. He, X. Zhang, S. Ren, and J. Sun. Delving deep into rectifiers: Surpassing human-level performance on imagenet classification. In *Proc. of the IEEE International Conf. on Computer Vision (ICCV)*, 2015. 4
- [23] M. Heusel, H. Ramsauer, T. Unterthiner, B. Nessler, and S. Hochreiter. Gans trained by a two time-scale update rule converge to a local nash equilibrium. In *Advances in Neural Information Processing Systems (NIPS)*, 2017. 4, 5, 6
- [24] J. Howard and S. Ruder. Universal language model fine-tuning for text classification. In *Association for Computational Linguistics (ACL)*, 2018. 2
- [25] X. Huang, Y. Li, O. Poursaeed, J. Hopcroft, and S. Belongie. Stacked generative adversarial networks. In *Proc. IEEE Conf. on Computer Vision and Pattern Recognition (CVPR)*, 2017. 2
- [26] D. A. Hudson and C. L. Zitnick. Generative adversarial transformers. *arXiv.org*, 2103.01209, 2021. 6, 7, 8, 9, 30
- [27] Y. Jiang, S. Chang, and Z. Wang. Transgan: Two transformers can make one strong gan. *arXiv.org*, 2021. 21
- [28] J. Johnson, A. Alahi, and L. Fei-Fei. Perceptual losses for real-time style transfer and super-resolution. In *Proc. of the European Conf. on Computer Vision (ECCV)*, 2016. 2
- [29] J. Johnson, B. Hariharan, L. van der Maaten, L. Fei-Fei, C. Lawrence Zitnick, and R. Girshick. Clevr: A diagnostic dataset for compositional language and elementary visual reasoning. In *Proc. IEEE Conf. on Computer Vision and Pattern Recognition (CVPR)*, 2017. 7
- [30] A. Karnewar and O. Wang. Msg-gan: Multi-scale gradients for generative adversarial networks. In *Proc. IEEE Conf. on Computer Vision and Pattern Recognition (CVPR)*, 2020. 2, 21
- [31] T. Karras, T. Aila, S. Laine, and J. Lehtinen. Progressive growing of GANs for improved quality, stability, and variation. In *Proc. of the International Conf. on Learning Representations (ICLR)*, 2018. 2, 16, 30

- [32] T. Karras, M. Aittala, J. Hellsten, S. Laine, J. Lehtinen, and T. Aila. Training generative adversarial networks with limited data. In *Advances in Neural Information Processing Systems (NeurIPS)*, 2020. [2](#), [3](#), [4](#), [6](#), [7](#), [9](#), [18](#), [19](#), [20](#), [22](#), [29](#), [31](#)
- [33] T. Karras, S. Laine, and T. Aila. A style-based generator architecture for generative adversarial networks. In *Proc. IEEE Conf. on Computer Vision and Pattern Recognition (CVPR)*, 2019. [1](#), [2](#), [6](#), [8](#), [9](#)
- [34] T. Karras, S. Laine, M. Aittala, J. Hellsten, J. Lehtinen, and T. Aila. Analyzing and improving the image quality of StyleGAN. In *Proc. IEEE Conf. on Computer Vision and Pattern Recognition (CVPR)*, 2020. [2](#), [6](#)
- [35] T. Karras, S. Laine, M. Aittala, J. Hellsten, J. Lehtinen, and T. Aila. Analyzing and improving the image quality of StyleGAN. 2020. [18](#)
- [36] A. Khosla, N. Jayadevaprakash, B. Yao, and F.-F. Li. Novel dataset for fine-grained image categorization: Stanford dogs. In *Proc. IEEE Conf. on Computer Vision and Pattern Recognition (CVPR) Workshops*, 2011. [17](#)
- [37] D. P. Kingma and J. Ba. Adam: A method for stochastic optimization. In *Proc. of the International Conf. on Learning Representations (ICLR)*, 2015. [30](#)
- [38] D. P. Kingma and P. Dhariwal. Glow: Generative flow with invertible 1x1 convolutions. In *Advances in Neural Information Processing Systems (NeurIPS)*, 2018. [4](#)
- [39] D. P. Kingma and M. Welling. Auto-encoding variational bayes. *arXiv.org*, abs/1312.6114, 2013. [16](#)
- [40] A. Kolesnikov, L. Beyer, X. Zhai, J. Puigcerver, J. Yung, S. Gelly, and N. Houlsby. Big transfer (bit): General visual representation learning. In *Proc. of the European Conf. on Computer Vision (ECCV)*, 2020. [1](#)
- [41] S. Kornblith, J. Shlens, and Q. V. Le. Do better imagenet models transfer better? In *Proc. IEEE Conf. on Computer Vision and Pattern Recognition (CVPR)*, 2019. [1](#)
- [42] J. Krause, M. Stark, J. Deng, and L. Fei-Fei. 3D object representations for fine-grained categorization. In *Proc. of the IEEE International Conf. on Computer Vision (ICCV) Workshops*, 2013. [17](#)
- [43] K. Kurach, M. Lucic, X. Zhai, M. Michalski, and S. Gelly. The gan landscape: Losses, architectures, regularization, and normalization. In *Proc. of the International Conf. on Machine learning (ICML) Workshops*, 2018. [1](#)
- [44] T. Kynkäänniemi, T. Karras, S. Laine, J. Lehtinen, and T. Aila. Improved precision and recall metric for assessing generative models. *Advances in Neural Information Processing Systems (NeurIPS)*, 2019. [16](#)
- [45] C. Ledig, L. Theis, F. Huszar, J. Caballero, A. Cunningham, A. Acosta, A. P. Aitken, A. Tejani, J. Totz, Z. Wang, and W. Shi. Photo-realistic single image super-resolution using a generative adversarial network. In *Proc. IEEE Conf. on Computer Vision and Pattern Recognition (CVPR)*, 2017. [2](#)
- [46] Y. Liao, J. Xie, and A. Geiger. Kitti-360: A novel dataset and benchmarks for urban scene understanding in 2d and 3d. *arXiv.org*, 2109.13410, 2021. [17](#)
- [47] J. H. Lim and J. C. Ye. Geometric gan. *arXiv.org*, 1705.02894, 2017. [4](#)
- [48] T. Lin, P. Dollár, R. B. Girshick, K. He, B. Hariharan, and S. J. Belongie. Feature pyramid networks for object detection. In *Proc. IEEE Conf. on Computer Vision and Pattern Recognition (CVPR)*, 2017. [2](#)
- [49] B. Liu, Y. Zhu, K. Song, and A. Elgammal. Towards faster and stabilized gan training for high-fidelity few-shot image synthesis. In *Proc. of the International Conf. on Learning Representations (ICLR)*, 2021. [4](#), [6](#), [8](#), [9](#), [18](#), [19](#), [20](#), [21](#), [31](#)
- [50] L. Mescheder, A. Geiger, and S. Nowozin. Which training methods for gans do actually converge? In *Proc. of the International Conf. on Machine learning (ICML)*, 2018. [1](#), [31](#)
- [51] T. Miyato, T. Kataoka, M. Koyama, and Y. Yoshida. Spectral normalization for generative adversarial networks. In *Proc. of the International Conf. on Learning Representations (ICLR)*, 2018. [3](#)
- [52] S. Mo, M. Cho, and J. Shin. Freeze the discriminator: a simple baseline for fine-tuning gans. In *Proc. IEEE Conf. on Computer Vision and Pattern Recognition (CVPR) Workshops*, 2020. [2](#)
- [53] S. Morozov, A. Voynov, and A. Babenko. On self-supervised image representations for GAN evaluation. In *Proc. of the International Conf. on Learning Representations (ICLR)*, 2021. [6](#), [16](#)
- [54] B. Neyshabur, S. Bhojanapalli, and A. Chakrabarti. Stabilizing gan training with multiple random projections. *arXiv.org*, 1705.0783, 2017. [2](#), [3](#), [15](#)

- [55] A. Nguyen, J. Yosinski, Y. Bengio, A. Dosovitskiy, and J. Clune. Plug & play generative networks: Conditional iterative generation of images in latent space. *arXiv.org*, 1612.00005, 2016. 2
- [56] M.-E. Nilsback and A. Zisserman. Automated flower classification over a large number of classes. In *Proc. Indian Conf. on Computer Vision, Graphics & Image Processing*, 2008. 8, 17
- [57] T. Park, M.-Y. Liu, T.-C. Wang, and J.-Y. Zhu. Semantic image synthesis with spatially-adaptive normalization. In *Proc. IEEE Conf. on Computer Vision and Pattern Recognition (CVPR)*, 2019. 2
- [58] O. Patashnik, Z. Wu, E. Shechtman, D. Cohen-Or, and D. Lischinski. Styleclip: Text-driven manipulation of stylegan imagery. *arXiv.org*, 2103.17249, 2021. 2
- [59] M. E. Peters, M. Neumann, M. Iyyer, M. Gardner, C. Clark, K. Lee, and L. Zettlemoyer. Deep contextualized word representations. In *Conf. of the North American Chapter of the Association for Computational Linguistics (NAACL)*, 2018. 2
- [60] A. Radford, J. W. Kim, C. Hallacy, A. Ramesh, G. Goh, S. Agarwal, G. Sastry, A. Askell, P. Mishkin, J. Clark, et al. Learning transferable visual models from natural language supervision. *arXiv.org*, 2103.00020, 2021. 4, 16
- [61] A. Radford, K. Narasimhan, T. Salimans, and I. Sutskever. Improving language understanding by generative pre-training, 2018. 2
- [62] R. Ranftl, K. Lasinger, D. Hafner, K. Schindler, and V. Koltun. Towards robust monocular depth estimation: Mixing datasets for zero-shot cross-dataset transfer. *IEEE Trans. on Pattern Analysis and Machine Intelligence (PAMI)*, 2020. 1, 31
- [63] S. R. Richter, H. A. AlHaija, and V. Koltun. Enhancing photorealism enhancement. *arXiv.org*, 2105.04619, 2021. 2
- [64] E. Robb, W.-S. Chu, A. Kumar, and J.-B. Huang. Few-shot adaptation of generative adversarial networks. *arXiv.org*, 2010.11943, 2020. 17
- [65] O. Ronneberger, P. Fischer, and T. Brox. U-net: Convolutional networks for biomedical image segmentation. In *Medical Image Computing and Computer-Assisted Intervention (MICCAI)*, 2015. 4
- [66] M. S. Sajjadi, O. Bachem, M. Lucic, O. Bousquet, and S. Gelly. Assessing generative models via precision and recall. In *Advances in Neural Information Processing Systems (NeurIPS)*, 2018. 6, 16
- [67] M. S. Sajjadi, B. Scholkopf, and M. Hirsch. Enhancenet: Single image super-resolution through automated texture synthesis. In *Proc. of the IEEE International Conf. on Computer Vision (ICCV)*, 2017. 2
- [68] C. N. d. Santos, Y. Mroueh, I. Padhi, and P. Dognin. Learning implicit generative models by matching perceptual features. In *Proc. of the IEEE International Conf. on Computer Vision (ICCV)*, 2019. 2
- [69] A. Sauer and A. Geiger. Counterfactual generative networks. In *Proc. of the International Conf. on Learning Representations (ICLR)*, 2021. 2
- [70] E. Schonfeld, B. Schiele, and A. Khoreva. A u-net based discriminator for generative adversarial networks. In *Proc. IEEE Conf. on Computer Vision and Pattern Recognition (CVPR)*, 2020. 2
- [71] A. Shocher, Y. Gandelsman, I. Mosseri, M. Yarom, M. Irani, W. T. Freeman, and T. Dekel. Semantic pyramid for image generation. In *Proc. IEEE Conf. on Computer Vision and Pattern Recognition (CVPR)*, 2020. 2
- [72] Z. Si and S.-C. Zhu. Learning hybrid image templates (hit) by information projection. *IEEE Trans. on Pattern Analysis and Machine Intelligence (PAMI)*, 2011. 8
- [73] K. Simonyan and A. Zisserman. Very deep convolutional networks for large-scale image recognition. In *Proc. of the International Conf. on Learning Representations (ICLR)*, 2015. 2
- [74] K. K. Singh, U. Ojha, and Y. J. Lee. Finegan: Unsupervised hierarchical disentanglement for fine-grained object generation and discovery. In *Proc. IEEE Conf. on Computer Vision and Pattern Recognition (CVPR)*, 2019. 21
- [75] D. Sungatullina, E. Zakharov, D. Ulyanov, and V. Lempitsky. Image manipulation with perceptual discriminators. In *Proc. of the European Conf. on Computer Vision (ECCV)*, 2018. 2, 5
- [76] C. Szegedy, W. Liu, Y. Jia, P. Sermanet, S. E. Reed, D. Anguelov, D. Erhan, V. Vanhoucke, and A. Rabinovich. Going deeper with convolutions. In *Proc. IEEE Conf. on Computer Vision and Pattern Recognition (CVPR)*, 2015. 4

- [77] M. Tan and Q. Le. Efficientnet: Rethinking model scaling for convolutional neural networks. In *Proc. of the International Conf. on Machine learning (ICML)*, 2019. 4
- [78] H. Touvron, M. Cord, M. Douze, F. Massa, A. Sablayrolles, and H. Jégou. Training data-efficient image transformers & distillation through attention. *arXiv.org*, 2012.12877, 2020. 4
- [79] N.-T. Tran, V.-H. Tran, N.-B. Nguyen, T.-K. Nguyen, and N.-M. Cheung. On data augmentation for gan training. *IEEE Trans. on Image Processing (TIP)*, 2021. 2, 4
- [80] C. Wah, S. Branson, P. Welinder, P. Perona, and S. Belongie. The Caltech-UCSD Birds-200-2011 Dataset. Technical Report CNS-TR-2011-001, California Institute of Technology, 2011. 17
- [81] T.-C. Wang, M.-Y. Liu, J.-Y. Zhu, A. Tao, J. Kautz, and B. Catanzaro. High-resolution image synthesis and semantic manipulation with conditional gans. In *Proc. IEEE Conf. on Computer Vision and Pattern Recognition (CVPR)*, 2018. 2
- [82] Y. Wang, C. Wu, L. Herranz, J. van de Weijer, A. Gonzalez-Garcia, and B. Raducanu. Transferring gans: generating images from limited data. In *Proc. of the European Conf. on Computer Vision (ECCV)*, 2018. 2
- [83] K. Xiao, L. Engstrom, A. Ilyas, and A. Madry. Noise or signal: The role of image backgrounds in object recognition. In *Proc. of the International Conf. on Learning Representations (ICLR)*, 2021. 10
- [84] F. Yu, A. Seff, Y. Zhang, S. Song, T. Funkhouser, and J. Xiao. Lsun: Construction of a large-scale image dataset using deep learning with humans in the loop. *arXiv.org*, 1506.03365, 2015. 4, 8, 17
- [85] N. Yu, G. Liu, A. Dundar, A. Tao, B. Catanzaro, L. Davis, and M. Fritz. Dual contrastive loss and attention for gans. *arXiv.org*, 2103.16748, 2021. 7, 9
- [86] H. Zhang, I. Goodfellow, D. Metaxas, and A. Odena. Self-attention generative adversarial networks. In *Proc. of the International Conf. on Machine learning (ICML)*, 2019. 2, 8, 9, 30
- [87] J. Zhao, M. Mathieu, and Y. LeCun. Energy-based generative adversarial network. In *Proc. of the International Conf. on Learning Representations (ICLR)*, 2017. 2
- [88] M. Zhao, Y. Cong, and L. Carin. On leveraging pretrained gans for generation with limited data. In *Proc. of the International Conf. on Machine learning (ICML)*, 2020. 2
- [89] S. Zhao, Z. Liu, J. Lin, J.-Y. Zhu, and S. Han. Differentiable augmentation for data-efficient gan training. In *Advances in Neural Information Processing Systems (NeurIPS)*, 2020. 2, 4, 7, 31
- [90] Z. Zhao, Z. Zhang, T. Chen, S. Singh, and H. Zhang. Image augmentations for gan training. *arXiv.org*, 2006.02595, 2020. 2, 4
- [91] B. Zhou, H. Zhao, X. Puig, S. Fidler, A. Barriuso, and A. Torralba. Scene parsing through ade20k dataset. In *Proc. IEEE Conf. on Computer Vision and Pattern Recognition (CVPR)*, 2017. 17
- [92] J.-Y. Zhu, T. Park, P. Isola, and A. A. Efros. Unpaired image-to-image translation using cycle-consistent adversarial networks. In *Proc. of the IEEE International Conf. on Computer Vision (ICCV)*, 2017. 2

Appendix A Proofs

As described in the paper, Projected GAN training can be formulated as follows

$$\min_G \max_{\{D_l\}} \sum_{l \in \mathcal{L}} \left(\mathbb{E}_{\mathbf{x}} [\log D_l(P_l(\mathbf{x}))] + \mathbb{E}_{\mathbf{z}} [\log(1 - D_l(P_l(G(\mathbf{z}))))] \right) \quad (3)$$

where $\{D_l\}$ is a set of independent discriminators operating on different feature projections. In the following, we first prove Theorem 1 for a deterministic projection. The second proof demonstrates the theorem's validity when training with stochastic differentiable augmentations.

Proof (deterministic). The following proof follows the consistency proofs in [54] and [20]. Let $\{P_l\}_{l \in \mathcal{L}}$ be a set of fixed feature projectors. Furthermore, let \mathbb{P}_T be the density of the true data distribution and \mathbb{P}_G the density of the distribution the generator G produces. As in Theorem 1, $P_l \circ T$ and $P_l \circ G$ are functional compositions of P_l and the true/generated data distribution. The minimax objective in (3) is then defined via

$$\min_G \max_{\{D_l\}} \sum_{l \in \mathcal{L}} V_l(D_l, G) \quad (4)$$

where

$$\begin{aligned} V_l(D_l, G) &= \mathbb{E}_{\mathbf{x} \sim \mathbb{P}_T} [\log D_l(P_l(\mathbf{x}))] + \mathbb{E}_{\mathbf{x} \sim \mathbb{P}_G} [\log(1 - D_l(P_l(\mathbf{x})))] \\ &= \mathbb{E}_{\mathbf{y} \sim \mathbb{P}_{P_l \circ T}} [\log D_l(\mathbf{y})] + \mathbb{E}_{\mathbf{y} \sim \mathbb{P}_{P_l \circ G}} [\log(1 - D_l(\mathbf{y}))] \\ &= \int_{\mathbf{y}} \mathbb{P}_{P_l \circ T}(\mathbf{y}) \log(D_l(\mathbf{y})) + \mathbb{P}_{P_l \circ G}(\mathbf{y}) \log(1 - D_l(\mathbf{y})) d\mathbf{y} \end{aligned} \quad (5)$$

In the following we derive the optimal discriminator for a fixed G . For any $(a, b) \in \mathbb{R}^2 \setminus \{(0, 0)\}$, the function $t \rightarrow a \log(t) + b \log(1-t)$ obtains its maximum in $[0, 1]$ at $\frac{a}{a+b}$ [20]. Since the discriminators do not need to be defined outside $\text{supp}(\mathbb{P}_{P_l \circ T}) \cup \text{supp}(\mathbb{P}_{P_l \circ G})$, the maximum $\max_{\{D_l\}} V_l(D_l, G)$ is achieved for

$$D_{l,G}^*(\mathbf{y}) = \frac{\mathbb{P}_{P_l \circ T}(\mathbf{y})}{\mathbb{P}_{P_l \circ T}(\mathbf{y}) + \mathbb{P}_{P_l \circ G}(\mathbf{y})} \quad (6)$$

where G is fixed. Assuming a perfect discriminator, the minimax objective can be reformulated as

$$C(G) = \max_{\{D_l\}} \sum_l V_l(G, D_l) = \sum_l V_l(G, D_{l,G}^*) \quad (7)$$

Following the arguments of [20] and in [54], we obtain

$$C(G) = -2|\mathcal{L}| \log(2) + 2 \sum_l JSD(\mathbb{P}_{P_l \circ T} || \mathbb{P}_{P_l \circ G}) \quad (8)$$

where JSD is the Jensen-Shannon divergence. Since the Jensen-Shannon divergence is non-negative and zero only in case of equality, the minimum is achieved iff $\mathbb{P}_{P_l \circ T} = \mathbb{P}_{P_l \circ G}$ for all l . This shows, that we achieve $\min_G C(G)$ iff $\mathbb{P}_{P_l \circ T} = \mathbb{P}_{P_l \circ G}$ for all l .

Proof (stochastic). We now show that the result above still holds when applying stochastic differentiable augmentations before the feature projections. Utilizing a stochastic augmentation $f_{\theta,l}$ before the projection through P_l , can be viewed as a functional composition, i.e. $P_{\theta,l} = P_l \circ f_{\theta,l}$. The parameter $\theta \sim \mathbb{P}_{\Theta}$ encompasses both the probability of applying the augmentation and its parameters, e.g., translation direction and magnitude. As in the deterministic case, the minimax objective is defined as

$$\min_G \max_{\{D_l\}} \sum_{l \in \mathcal{L}} V_l(D_l, G) \quad (9)$$

where

$$\begin{aligned} V_l(D_l, G) &= \mathbb{E}_{\mathbf{x} \sim \mathbb{P}_T} [\mathbb{E}_{\theta \sim \mathbb{P}_{\Theta}} [\log D_l(P_{\theta,l}(\mathbf{x}))]] + \mathbb{E}_{\mathbf{x} \sim \mathbb{P}_G} [\mathbb{E}_{\theta \sim \mathbb{P}_{\Theta}} [\log(1 - D_l(P_{\theta,l}(\mathbf{x})))]] \\ &= \mathbb{E}_{\theta \sim \mathbb{P}_{\Theta}} [\mathbb{E}_{\mathbf{x} \sim \mathbb{P}_T} [\log D_l(P_{\theta,l}(\mathbf{x}))] + \mathbb{E}_{\mathbf{x} \sim \mathbb{P}_G} [\log(1 - D_l(P_{\theta,l}(\mathbf{x})))]] \\ &= \mathbb{E}_{\theta \sim \mathbb{P}_{\Theta}} [\mathbb{E}_{\mathbf{y} \sim \mathbb{P}_{P_{\theta,l} \circ T}} [\log D_l(\mathbf{y})] + \mathbb{E}_{\mathbf{y} \sim \mathbb{P}_{P_{\theta,l} \circ G}} [\log(1 - D_l(\mathbf{y}))]] \\ &= \mathbb{E}_{\theta \sim \mathbb{P}_{\Theta}} \left[\int_{\mathbf{y}} \mathbb{P}_{P_{\theta,l} \circ T}(\mathbf{y}) \log(D_l(\mathbf{y})) + \mathbb{P}_{P_{\theta,l} \circ G}(\mathbf{y}) \log(1 - D_l(\mathbf{y})) d\mathbf{y} \right] \\ &= \int_{\mathbf{y}} \mathbb{E}_{\theta \sim \mathbb{P}_{\Theta}} [\mathbb{P}_{P_{\theta,l} \circ T}(\mathbf{y}) \log(D_l(\mathbf{y})) + \mathbb{P}_{P_{\theta,l} \circ G}(\mathbf{y}) \log(1 - D_l(\mathbf{y}))] d\mathbf{y} \end{aligned} \quad (10)$$

Using the same arguments as above, we obtain that the maximum $\max_{\{D_l\}} V_l(D_l, G)$ is achieved for

$$D_{l,G}^*(\mathbf{y}) = \frac{\mathbb{E}_{\theta \sim \mathbb{P}_\Theta} [\mathbb{P}_{P_{\theta,l} \circ T}(\mathbf{y})]}{\mathbb{E}_{\theta \sim \mathbb{P}_\Theta} [\mathbb{P}_{P_{\theta,l} \circ T}(\mathbf{y})] + \mathbb{E}_{\theta \sim \mathbb{P}_\Theta} [\mathbb{P}_{P_{\theta,l} \circ G}(\mathbf{y})]} \quad (11)$$

where G is fixed. Note that $\mathbb{E}_{\theta \sim \mathbb{P}_\Theta} [\mathbb{P}_{P_{\theta,l} \circ T}]$ and $\mathbb{E}_{\theta \sim \mathbb{P}_\Theta} [\mathbb{P}_{P_{\theta,l} \circ G}]$ are densities. Similar to above, we obtain $\min_G C(G)$ iff $\mathbb{E}_{\theta \sim \mathbb{P}_{\Theta,l}} [\mathbb{P}_{P_l \circ T}] = \mathbb{E}_{\theta \sim \mathbb{P}_\Theta} [\mathbb{P}_{P_{\theta,l} \circ G}]$ for all l .

Appendix B Additional Metrics and Datasets

Metrics. In addition to FID and *Imgs* reported in the paper, we compute the following metrics:

- **Kernel Inception Distance (KID) [4].** KID is an unbiased alternative to FID, hence, especially suitable for small datasets.
- **Precision and Recall [66].** Precision measures the quality of samples, and recall measures image diversity. Generally, GANs produce high-quality samples while being prone to mode collapse (high precision, low recall), compared to VAEs [39], which generate lower quality but more diverse samples (low precision, high recall). This observation is evidenced empirically in [66]. For our evaluation, we use the improved formulation by [44].
- **SwAV-FID [53].** Instead of utilizing an image classifier feature space, SwAV-FID uses self-supervised representations. More specifically, SwAV-FID computes the Fréchet distance in the penultimate layer of a ResNet-50 trained with the contrastive SwAV objective [6]. Morozov et al. [53] show that in some cases, SwAV-FID is more consistent with human judgment of visual quality than FID.
- **CLIP-FID & Vortex-FID.** FID uses an Inception network trained on ImageNet. Our feature network F has also been trained on ImageNet. To rule out training data as a confounding factor between F and the evaluation metric, we propose to use FID with non-ImageNet features. We evaluate CLIP-FID (using a ResNet50 trained with the CLIP objective on the dataset collected by [60]) and VirTex-FID (using a ResNet50 trained on COCO Captions with the VirTex objective [11]).
- **Sliced Wasserstein Distance (SWD).** SWD is a non-neural metric that computes the Wasserstein distance between local image patches drawn from a Laplacian pyramid. We follow the evaluation protocol proposed by [31].

In addition to the metrics above, we conduct a **human preference study** with 28 participants unfamiliar with our method. The structure of the study is as follows:

- For each dataset, we first show samples of the real dataset for context.
- We then present two sample sheets and ask the participants to rank the sheets relative to each other based on sample fidelity and diversity. We define these as follows: (i) Fidelity is the degree to which the generated samples resemble the real ones. (ii) Diversity measures whether the generated samples cover the full variability of the real samples.
- Each sheet contains nine random samples; we present three sample sheet pairs per dataset.
- Samples and comparison pairs are randomized per participant. We make sure that all possible pairings are equally represented.
- Evaluated Models: StyleGAN2-ADA, FastGAN, Projected GAN, and real data (for control)
- Evaluated datasets: all 256x256 datasets
- We count how often a given model wins a comparison and report the relative amount of wins.

Results. On all datasets, KID, SwAV-FID, CLIP-FID, VirTex-FID, and SWD mirror the ranking obtained via FID. The low SwAV-FIDs indicate that Projected GAN’s low FIDs are not due to correlations between the feature network used for projection and the inception network used in FID.

On the large datasets, the baselines only outperform Projected GAN in precision on FFHQ, Cityscapes, and LSUN Church (Table 4). However, when comparing recall in these cases, it is apparent that the baselines suffer from mode collapse. The high recall generally obtained by Projected GAN hints at the reason for its superior performance on FID, KID, and SwAV-FID: the generated images are very

diverse. Hence, we conclude that Projected GANs alleviate mode collapse. The sample diversity is also evident in the qualitative comparisons in Section C. On small datasets (Table 5), Projected GAN is outperformed in precision on Art Painting by FastGAN; however, FastGANs very low recall of 0.044 hints at mode collapse. Only on flowers, Projected GAN appears to cover fewer modes than the baselines as indicated by lower recall.

At high resolutions (Table 6), Projected GAN performs slightly worse in precision. It appears that Projected GAN incurs small losses in image quality while obtaining a better mode coverage, which can be observed in the quantitative comparisons, e.g., on AFHQ-Cat, some samples exhibit artifacts. These artifacts indicate that projected GAN training at higher resolutions warrants closer inspection.

On small datasets, overfitting is a problem that is not detected well by FID and other metrics [64]. Therefore, it is instructive to inspect latent interpolations for which we refer the reader to the supplementary videos. Projected GAN generates smooth interpolations between random samples on all datasets suggesting that it generalizes rather than memorizing training samples.

The results of the human preference study are shown in Table 7. The study results largely agree with the results obtained via FID. On FFHQ, the study demonstrates our reported failure case for projected GANs. Interestingly, on AnimalFace projected GAN outperforms real data. We hypothesize that this is because for AnimalFace there is a significant portion of low-quality images (blurry, compression artifacts) in the dataset, and possibly projected GAN generates fewer of those. Of course, human studies are not optimal, as it is not straightforward to evaluate sample diversity - which is a strong suit of projected GANs - given only a few samples.

Table 8 reports the FID achieved by Projected GAN for nine more datasets, all at a resolution of 256^2 . We compare on LSUN cat and horse [84], ADE indoor (a subset of ADE [91] proposed in [3]), the full Oxford flowers dataset with 8k images [56], KITTI-fisheye (a subset of KITTI-360 [46], consisting of fisheye images), STL-10 [8], CUB200 [80], Stanford Dogs [36], and Stanford Cars [42]. We do not change the hyperparameters of Projected GAN. On each dataset, we report the lowest FID achieved in previous literature. We train FastGAN as a baseline for ADE indoor and KITTI-fisheye.

Large Datasets (256 ²)					
	CLEVR	FFHQ	Cityscapes	Bedroom	Church
<i>FID</i> ↓					
STYLEGAN2-ADA [32]	10.17	7.32	8.35	11.53	5.85
FASTGAN [49]	3.24	12.69	8.78	8.24	8.43
PROJECTED GAN	0.89	3.08	3.41	1.52	1.59
<i>KID</i> × 10 ³ ↓					
STYLEGAN2-ADA [32]	8.15	1.49	3.34	7.42	4.70
FASTGAN [49]	2.64	5.34	5.45	5.90	4.61
PROJECTED GAN	0.51	0.44	0.91	0.36	0.50
<i>Precision</i> ↑					
STYLEGAN2-ADA [32]	0.373	0.669	0.649	0.429	0.565
FASTGAN [49]	0.600	0.716	0.557	0.602	0.645
PROJECTED GAN	0.640	0.654	0.619	0.614	0.612
<i>Recall</i> ↑					
STYLEGAN2-ADA [32]	0.569	0.445	0.146	0.202	0.416
FASTGAN [49]	0.650	0.184	0.227	0.189	0.207
PROJECTED GAN	0.735	0.464	0.361	0.346	0.438
<i>SwAV – FID</i> ↓					
STYLEGAN2-ADA [32]	3.50	1.24	1.35	8.47	2.51
FASTGAN [49]	1.46	2.55	1.29	5.38	3.64
PROJECTED GAN	0.56	0.85	0.60	1.44	1.01
<i>CLIP – FID</i> ↓					
STYLEGAN2-ADA [32]	4.70	10.3	5.88	42.12	15.85
FASTGAN [49]	4.24	19.23	6.46	31.10	35.47
PROJECTED GAN	0.80	7.55	2.96	11.97	13.71
<i>VirTex – FID</i> ↓					
STYLEGAN2-ADA [32]	0.78	1.20	1.15	2.20	1.10
FASTGAN [49]	0.64	2.47	1.48	2.66	3.61
PROJECTED GAN	0.35	0.64	0.49	0.81	0.82
<i>SWD</i> × 10 ⁻³ ↓					
STYLEGAN2-ADA [32]	17.50	7.42	10.71	12.53	14.62
FASTGAN [49]	28.51	10.19	9.45	14.68	14.42
PROJECTED GAN	12.90	6.41	7.27	6.83	8.37

Table 4: **Metrics on Large Datasets (256²)**. Projected GAN compares favorably on most metrics. Exceptions are precision on FFHQ, Cityscapes, and LSUN Church. As argued by [35], shifting from precision to recall is generally desirable, since recall can be traded into precision via truncation.

Small Datasets (256 ²)					
	Art Painting	Landscape	AnimalFace	Flowers	Pokemon
<i>FID</i> ↓					
STYLEGAN2-ADA [32]	43.07	15.99	60.90	21.66	40.38
FASTGAN [49]	44.02	16.44	62.11	26.23	81.86
PROJECTED GAN	27.96	6.92	17.88	13.86	26.36
<i>KID</i> × 10 ³ ↓					
STYLEGAN2-ADA [32]	10.23	4.39	22.52	3.56	13.49
FASTGAN [49]	13.00	3.40	22.11	6.61	80.30
PROJECTED GAN	1.25	1.30	0.03	0.38	1.32
<i>Precision</i> ↑					
STYLEGAN2-ADA [32]	0.691	0.709	0.841	0.731	0.735
FASTGAN [49]	0.858	0.768	0.849	0.611	0.731
PROJECTED GAN	0.762	0.774	0.998	0.816	0.809
<i>Recall</i> ↑					
STYLEGAN2-ADA [32]	0.218	0.213	0.036	0.095	0.197
FASTGAN [49]	0.044	0.160	0.015	0.100	0.004
PROJECTED GAN	0.239	0.258	0.095	0.058	0.259
<i>SwAV – FID</i> ↓					
STYLEGAN2-ADA [32]	3.32	2.98	16.26	5.02	6.71
FASTGAN [49]	3.29	2.42	15.07	7.45	9.25
PROJECTED GAN	2.25	1.42	4.22	2.70	2.04
<i>CLIP – FID</i> ↓					
STYLEGAN2-ADA [32]	44.13	24.89	46.18	26.30	13.96
FASTGAN [49]	40.47	19.84	54.69	40.12	87.65
PROJECTED GAN	22.91	13.71	16.89	15.83	9.93
<i>VirTex – FID</i> ↓					
STYLEGAN2-ADA [32]	4.15	2.78	8.83	3.25	3.69
FASTGAN [49]	5.72	3.86	9.41	4.08	17.49
PROJECTED GAN	3.53	1.98	3.79	2.19	2.55
<i>SWD</i> × 10 ⁻³ ↓					
STYLEGAN2-ADA [32]	25.55	19.06	22.31	14.04	14.73
FASTGAN [49]	21.94	29.87	29.23	17.39	46.81
PROJECTED GAN	11.44	15.38	14.34	9.61	11.65

Table 5: **Metrics on Small Datasets** (256²). Projected GAN performs best on most metrics.

	1024 ²		512 ²		
	Art Painting	Pokemon	AHFQ-Cat	AFHQ-Dog	AFHQ-Wild
	<i>FID</i> ↓				
STYLEGAN2-ADA [32]	41.69	56.76	3.55	7.40	3.05
FASTGAN [49]	46.71	56.46	4.69	13.09	3.14
PROJECTED GAN	32.07	33.96	2.16	4.52	2.17
	<i>KID</i> × 10 ³ ↓				
STYLEGAN2-ADA [32]	26.59	15.31	0.63	1.21	0.47
FASTGAN [49]	12.70	29.40	1.72	5.51	0.74
PROJECTED GAN	1.70	7.76	0.16	0.80	0.12
	<i>Precision</i> ↑				
STYLEGAN2-ADA [32]	0.619	0.791	0.767	0.753	0.765
FASTGAN [49]	0.776	0.777	0.784	0.746	0.761
PROJECTED GAN	0.706	0.780	0.693	0.718	0.705
	<i>Recall</i> ↑				
STYLEGAN2-ADA [32]	0.168	0.053	0.411	0.470	0.137
FASTGAN [49]	0.033	0.080	0.305	0.380	0.201
PROJECTED GAN	0.235	0.215	0.565	0.643	0.292
	<i>SwAV – FID</i> ↓				
STYLEGAN2-ADA [32]	3.68	5.03	1.23	1.98	1.89
FASTGAN [49]	3.41	5.14	1.73	3.07	1.77
PROJECTED GAN	2.28	3.83	0.68	1.12	1.08

Table 6: **Metrics on Small Datasets** (512² and 1024²). The results are in line with the findings at a resolution of 256². Only with respect to precision, the baselines slightly outperform Projected GAN.

	CLEVR	FFHQ	Cityscapes	Bedroom	Church	ArtPainting	Landscape	AnimalFace	Flowers	Pokemon	All Datasets
	Fidelity										
STYLEGAN2-ADA [32]	14 %	32 %	17 %	5 %	16 %	16 %	21 %	4 %	17 %	10 %	15 %
FASTGAN [49]	7 %	2 %	15 %	3 %	9 %	0 %	8 %	7 %	4 %	0 %	6 %
PROJECTED GAN	42 %	5 %	15 %	16 %	9 %	28 %	17 %	55 %	25 %	38 %	25 %
DATA	37 %	61 %	53 %	76 %	66 %	56 %	54 %	34 %	54 %	52 %	54 %
	Diversity										
STYLEGAN2-ADA [32]	13 %	24 %	9 %	10 %	19 %	11 %	25 %	9 %	17 %	6 %	14 %
FASTGAN [49]	13 %	4 %	11 %	2 %	0 %	4 %	13 %	9 %	17 %	0 %	7 %
PROJECTED GAN	31 %	12 %	21 %	21 %	14 %	27 %	16 %	49 %	29 %	40 %	27 %
DATA	43 %	60 %	59 %	67 %	67 %	58 %	46 %	33 %	37 %	54 %	52 %

Table 7: **Human Preference Study**. The obtained results largely agree with the rankings of other metrics.

	LSUN cat	LSUN horse	ADE indoor	Flowers Full	KITTI fisheye
Prev. SotA (Approach)	5.57 (ADM [12])	2.57 (ADM [12])	30.33 (FastGAN [49])	19.60 (MSG-StyleGAN [30])	6.64 (FastGAN [49])
Projected GAN	3.89	2.17	6.70	3.86	2.72

	STL-10	CUB200	Stanford Dogs	Stanford Cars
Prev. SotA (Approach)	25.32 (TransGAN [27])	11.25 (FineGAN [74])	25.66 (FineGAN [74])	16.03 (FineGAN [74])
Projected GAN	13.68	2.79	11.75	2.09

Table 8: **FID on Additional Datasets** (256^2) Without any hyperparameter changes, Projected GAN outperforms the previous state-of-the art on all evaluated datasets.

Appendix C Qualitative Comparisons

We show generated images for CLEVR (Fig. 9), FFHQ (Fig. 10), Cityscapes (Fig. 11), Bedroom (Fig. 12), Church (Fig. 13), Art Painting (Fig. 14, 19), Landscape (Fig. 15), AnimalFace Dog (Fig. 16), Flowers (Fig. 17), Pokemon (Fig. 18, 20), AFHQ-Cat (Fig. 21), AFHQ-Dog (Fig. 22), and AFHQ-Wild (Fig. 23). Following [32], we select a global seed per dataset. We do not perform truncation on any of the models. Projected GAN produces convincing results on all datasets. The sample diversity in particular is apparent in comparison to the baselines, e.g., on AFHQ-Cat or AFHQ-Wild, all baselines generate high-quality samples, but Projected GAN captures more variability of the training data.

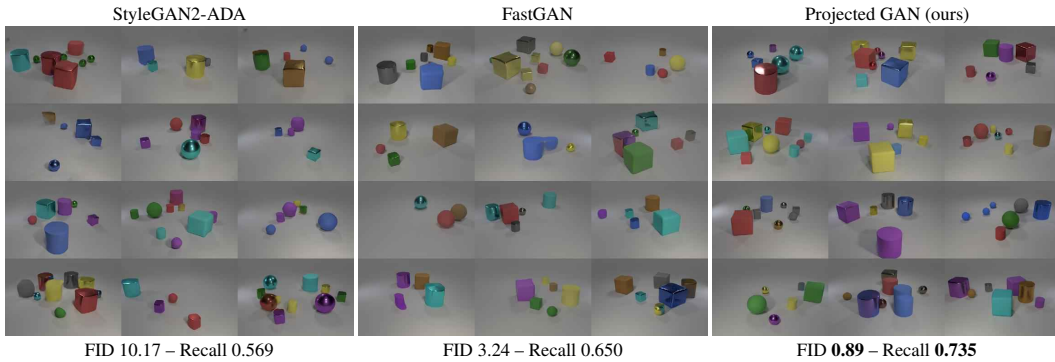


Figure 9: **Uncurated Results for CLEVR** (256^2). The images are selected randomly given one global random seed. We recommend zooming in for comparison.



Figure 10: **Uncurated Results for FFHQ** (256^2). The images are selected randomly given one global random seed. We recommend zooming in for comparison.



Figure 11: **Uncurated Results for Cityscapes (256^2)**. The images are selected randomly given one global random seed. We recommend zooming in for comparison.



Figure 12: **Uncurated Results for LSUN bedroom (256^2)**. The images are selected randomly given one global random seed. We recommend zooming in for comparison.

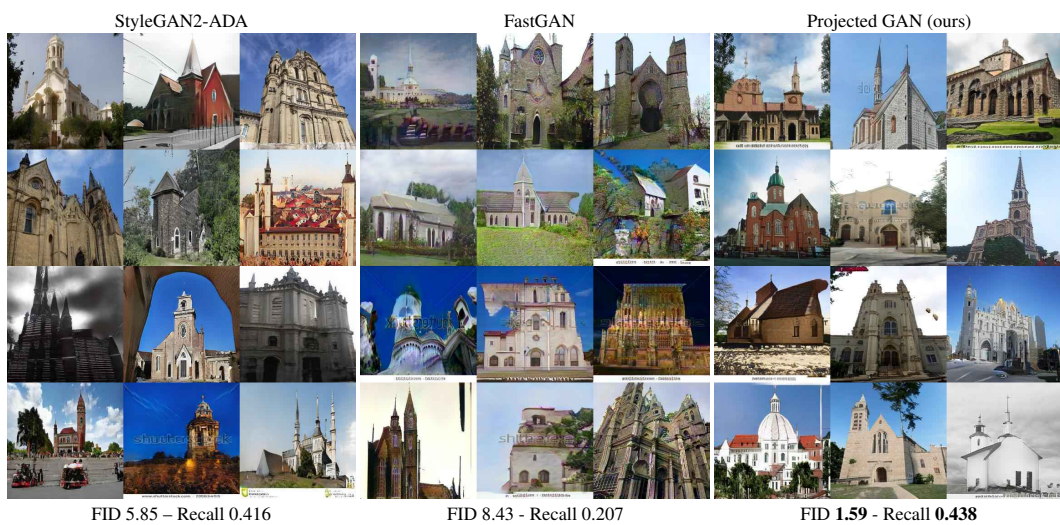


Figure 13: **Uncurated Results for LSUN church (256^2)**. The images are selected randomly given one global random seed. We recommend zooming in for comparison.

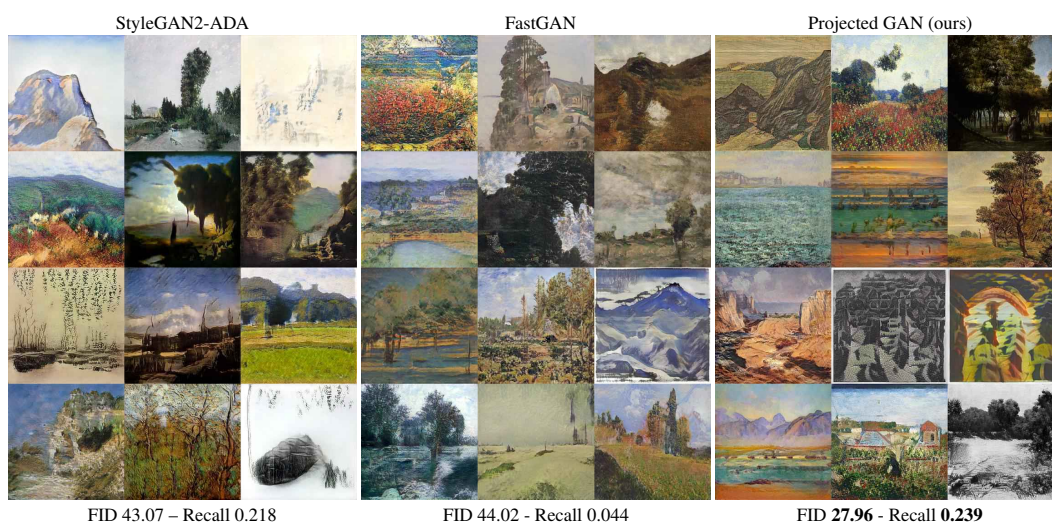


Figure 14: **Uncurated Results for Art Painting** (256^2). The images are selected randomly given one global random seed. We recommend zooming in for comparison.

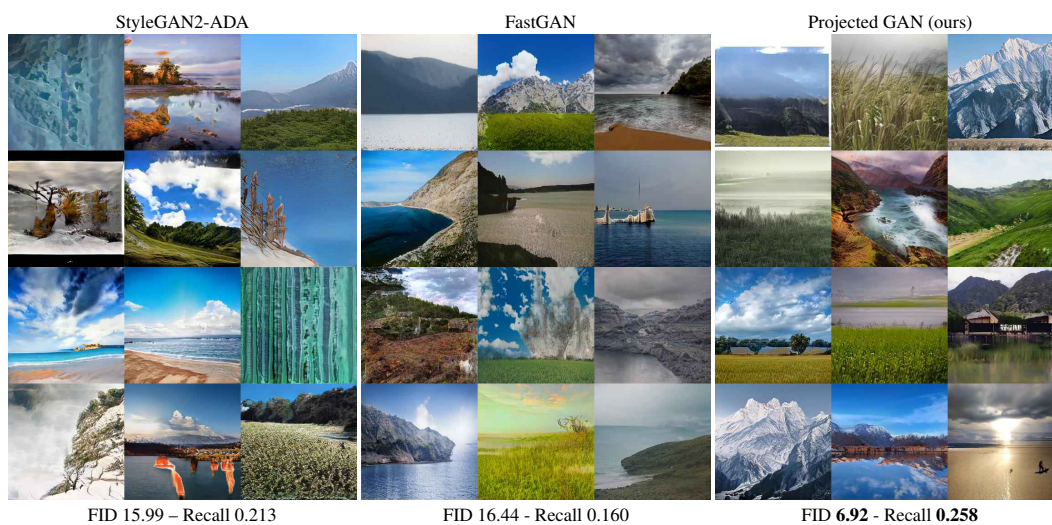


Figure 15: **Uncurated Results for Landscape** (256^2). The images are selected randomly given one global random seed. We recommend zooming in for comparison.

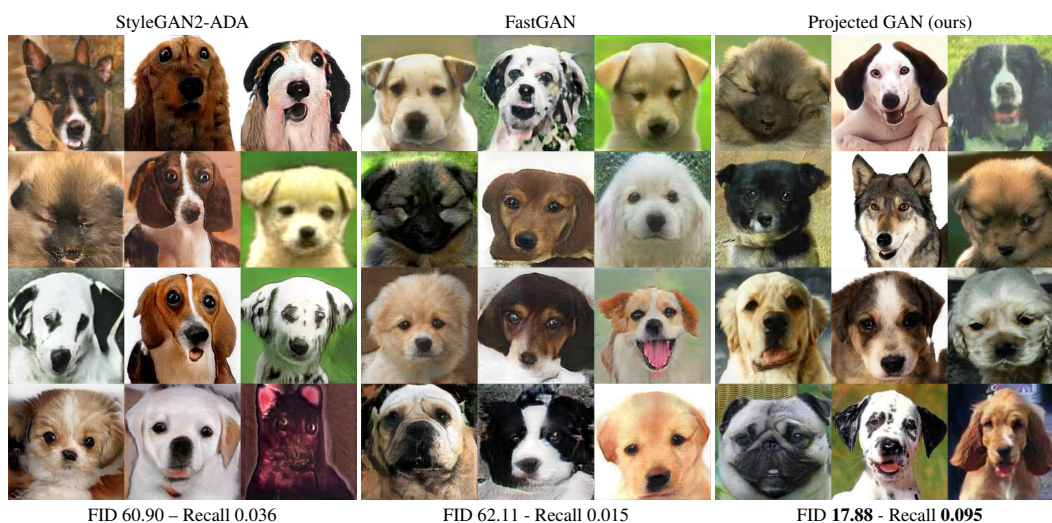


Figure 16: **Uncurated Results for AnimalFace-Dog (256^2)**. The images are selected randomly given one global random seed. We recommend zooming in for comparison.

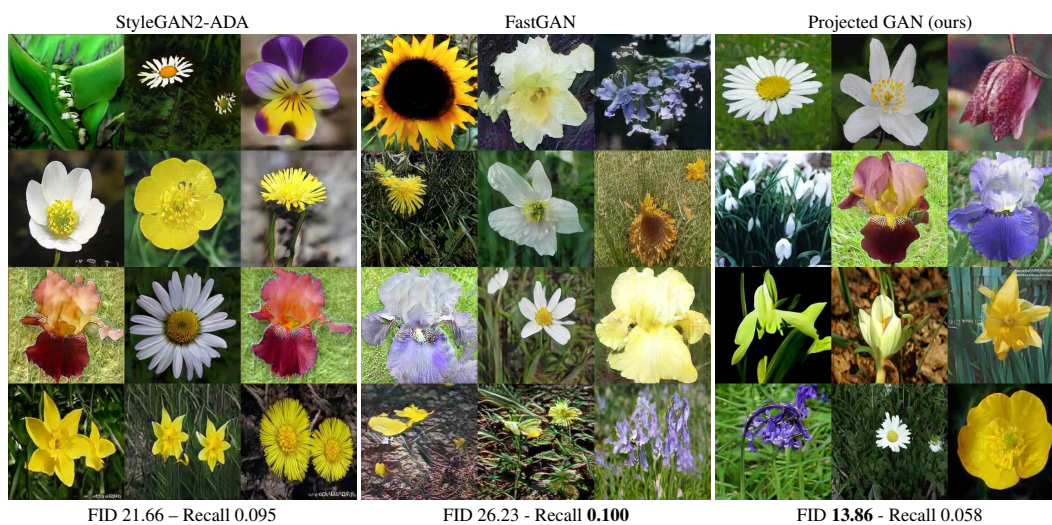


Figure 17: **Uncurated Results for Flowers (256^2)**. The images are selected randomly given one global random seed. We recommend zooming in for comparison.



Figure 18: **Uncurated Results for Pokemon** (256^2). The images are selected randomly given one global random seed. We recommend zooming in for comparison.

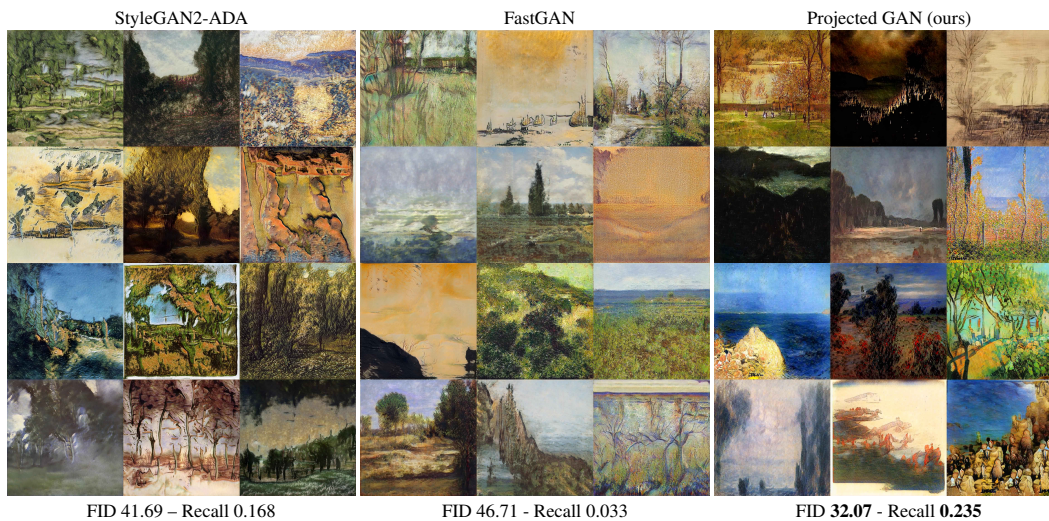


Figure 19: **Uncurated Results for Art Painting** (1024^2). The images are selected randomly given one global random seed. We recommend zooming in for comparison.

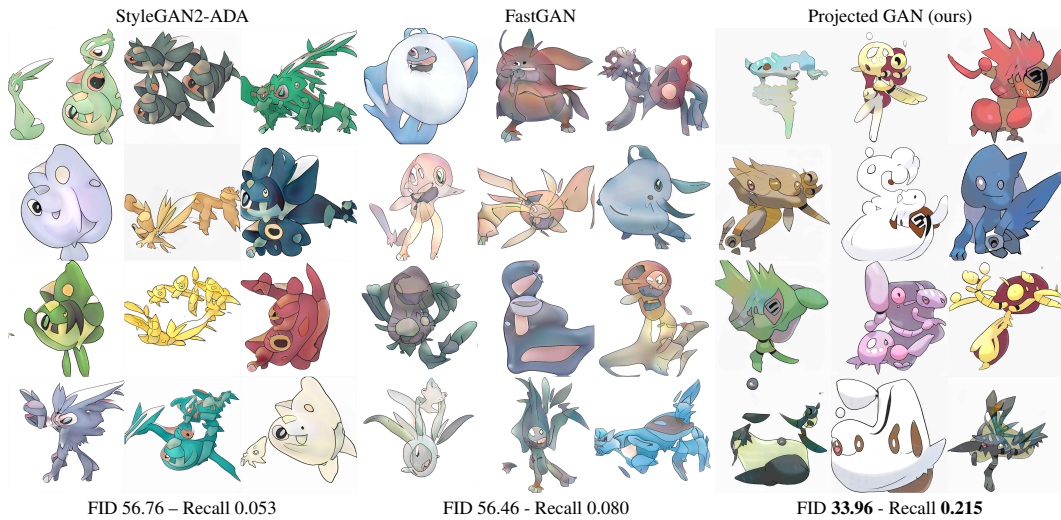


Figure 20: **Uncurated Results for Pokemon** (1024^2). The images are selected randomly given one global random seed. We recommend zooming in for comparison.

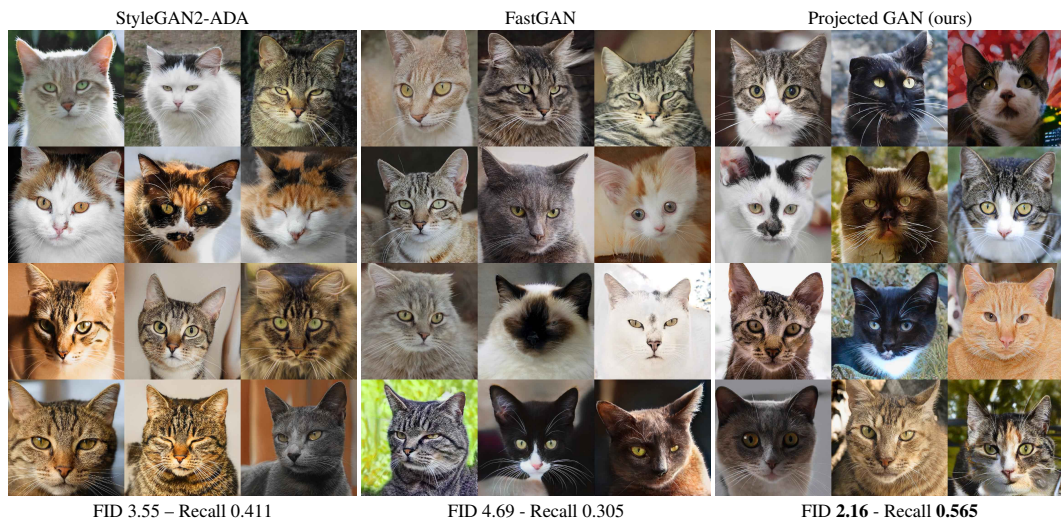


Figure 21: **Uncurated Results for AFHQ-Cat** (512^2). The images are selected randomly given one global random seed. We recommend zooming in for comparison.

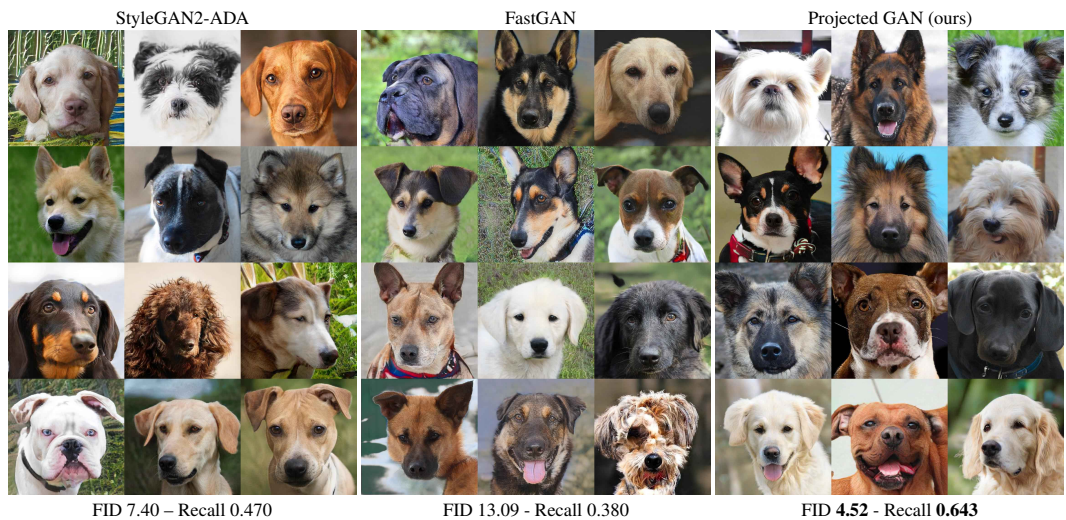


Figure 22: **Uncurated Results for AFHQ-Dog** (512^2). The images are selected randomly given one global random seed. We recommend zooming in for comparison.

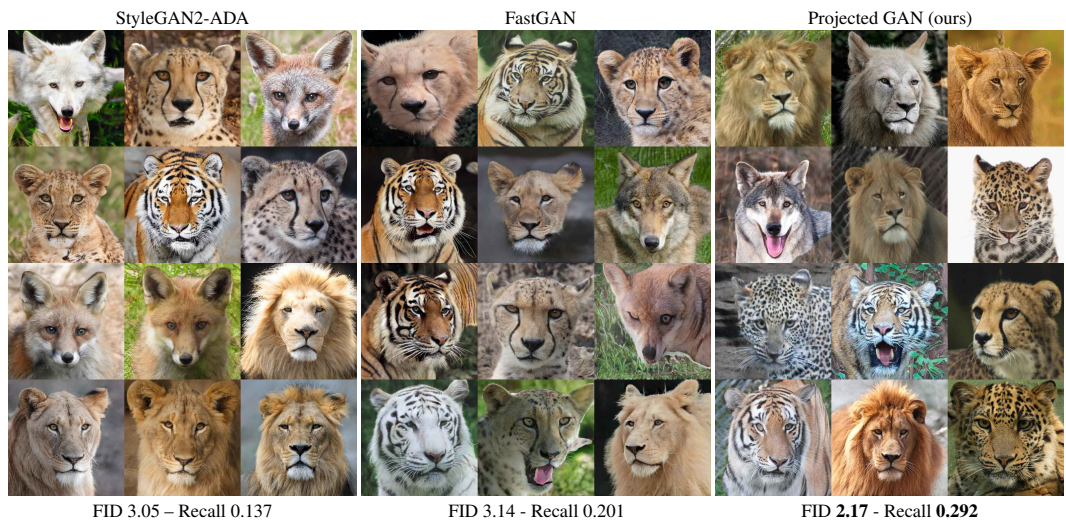


Figure 23: **Uncurated Results for AFHQ-Wild** (512^2). The images are selected randomly given one global random seed. We recommend zooming in for comparison.

Appendix D Additional Experiments

This section presents additional experiments referenced in the paper. The experiments explore alternative setups to our final configuration entailing a pretrained, fixed feature network F , fixed 1x1 convolutions for cross-channel mixing (CCM), and fixed convolutions for cross-scale mixing (CSM). We follow the setup of Section 4 of the paper: training on LSUN church at a resolution of 256^2 , with a batch size of 64 for 1 million *Imgs*, four discriminators, and a EfficientNet-Lite1 as feature network F . Again, we report FID normalized by the FID obtained by a model with a standard single RGB image discriminator. Values > 1 indicate worse performance than the RGB baseline. The results are summarized in Table 9.

No Projection. In all experiments, we utilize pretrained representations. As a sanity check, it is instructive to test if the architectural bias of F alone is helpful. The results in Table 9 demonstrate that randomly initializing F results in much higher FID.

CCM. We explore three different options for CCM. The first option, *Feature Norm*, does not mix features; rather, it normalizes the features to exhibit zero mean and a standard deviation of 1. This option investigates the importance of input scaling. The two other options utilize random convolution with different initializations. *CCM-rotation* is initialized with a random rotation matrix, *CCM-Kaiming* utilizes Kaiming initialization. As shown in Table 9, *CCM-Kaiming* (0.77) improves over the baselines (*Feature Norm* (1.27), *CCM-rotation* (1.27)), over the RGB baseline (1.0), and pretrained F without projection (1.15). This supports our hypothesis, that we need a sufficient amount of channel mixing.

CSM. We investigate if training the random projections P_{rand} in CCM and CSM is advantageous for FID. We consider two options: training P_{rand} before or during GAN training. First, we train P_{rand} before GAN training, the feature network F remains fixed. For this purpose, we add a head on the last CSM layer to map back to full resolution and three output channels, forming an autoencoder architecture. This model trains with a denoising autoencoder loss on ImageNet: the input image is augmented with gaussian blur, JPEG compression, coarse and fine region dropout, and conversion to grayscale. All augmentations are applied with a probability of 0.5. The target for reconstruction is the non-augmented image. We keep four models, at the beginning of training (t_0), at convergence (t_3), and two in between with equal spacing in terms of reconstruction loss. After autoencoder training, we use the model (without the additional head) for projected GAN training, denoted as *Denoising AE* (t_i). Interestingly, the longer the AE trained, the higher the FID, see Table 9. For the second ablation, different parts of the projection stay fixed during GAN training: (i) training both F and P_{rand} , (ii) fixed F , training only P_{rand} , (iii) both F and P_{rand} stay fixed. Again, the results in Table 9 suggest that training any part of the projection results in worse performance. We conclude that training the random projection is not advantageous, neither before nor during GAN training.

The signed real logits of the discriminator $sign(D(\mathbf{x}))$ are the portion of the training set that gets positive discriminator outputs. Karras et al. [32] find this a helpful heuristic for quantifying discriminator overfitting. The signed logits should remain constant, which they achieve via adapting the augmentation probability during training. Fig. 24 shows that the logits of the RGB baseline steadily increase throughout training, whereas the logits remain mostly constant for Projected GAN training. This observation coincides with the finding that adaptive augmentation is unnecessary for Projected GANs as the logits are already stable.

Configuration	FID
No Projection	
Random F	11.03
Pretrained F	1.15
CCM	
Feature Norm	1.27
CCM-rotation	1.27
CCM-Kaiming	0.77
CCM + CSM	
Denoising AE (t_0)	0.24
Denoising AE (t_1)	0.37
Denoising AE (t_2)	0.44
Denoising AE (t_3)	0.59
Train F , Train P_{rand}	3.09
Fixed F , Train P_{rand}	0.97
Fixed F , Fixed P_{rand}	0.24

Table 9: **Ablations.**

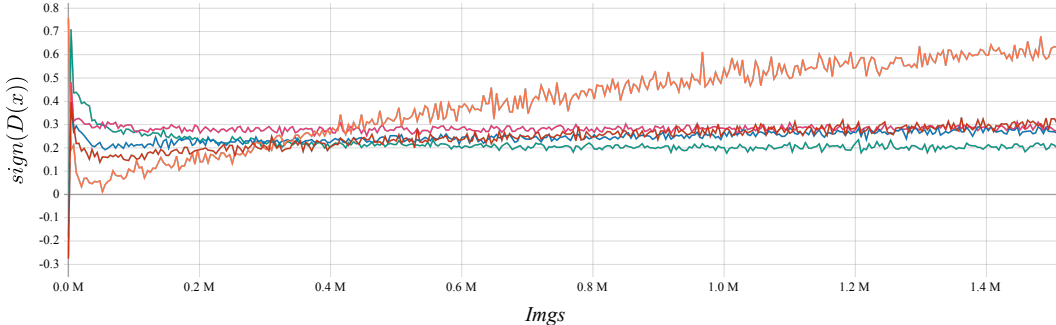


Figure 24: **Signed Discriminator Logits.** For this experiment, we project through F and train with up to four discriminators; we leave the augmentation probability constant. ($|D_i| = 1$: red, $|D_i| = 2$: blue, $|D_i| = 3$: pink, $|D_i| = 4$: green, RGB baseline: orange). For projected GAN training, the logits remain stable throughout training.

Appendix E Implementation Details

This section highlights the codebases we used and details hyperparameters and training configurations.

E.1 Code and Compute

For dataset preparation, training, and evaluation, we build on top of the StyleGAN2-ADA codebase¹. The evaluation employs the official pretrained Inception network to compute FID and KID. For SwAV-FID, we integrate the model of the SwAV-FID codebase² using weights by [6]. SAGAN [86] and Gansformers [26] are trained in the Gansformers codebase³, we use their default hyperparameters. For the feature networks’ implementation and weights, we use timm⁴, except for R50-CLIP⁵. Lastly, we utilize official implementations for differentiable augmentation⁶ and FastGAN⁷.

We conduct our experiments on an internal cluster with several nodes, each with up to 8 Quadro RTX 6000 or NVIDIA V100 using PyTorch 1.7.1 and CUDA 11.0.

E.2 Wall Clock-Time

On images at resolution 256^2 , the wall-clock training times measured in sec/king using 8 Quadro RTX 6000 are shown in Table 10. StyleGAN2 is the fastest overall, which is expected as we enable mixed-precision and use the custom CUDA kernels provided by the authors. These are not available for the FastGAN generator; hence, Projected GAN can only be compared to FastGAN in a fair manner. FastGANs wall-clock times are higher because it uses a reconstruction loss on the discriminator features. This reconstruction loss adds computational overhead. In contrast, projected GANs exhibit lower wall-clock times as we do not need any regularization other than spectral normalization.

Model	sec/king
STYLEGAN2-ADA	5.6
FASTGAN	7.2
PROJECTED GAN	10.1

Table 10: **Training Speed.**

E.3 Hyperparameters

Below, we describe the hyperparameter search for each method. For optimization, we always use Adam [37] with $\beta_1 = 0$, $\beta_2 = 0.99$, and $\epsilon = 10^{-8}$. All models employ exponential moving average for the generator weights [31].

StyleGAN2-ADA. The official codebase supplies standard configurations of architectures and hyperparameters for different resolutions. Furthermore, an automatic configuration option is available,

¹<https://github.com/NVLabs/stylegan2-ada-pytorch>

²<https://github.com/stanis-morozov/self-supervised-gan-eval/>

³<https://github.com/dorarad/gansformer>

⁴<https://github.com/rwightman/pytorch-image-models>

⁵<https://github.com/openai/CLIP>

⁶<https://github.com/mit-han-lab/data-efficient-gans>

⁷<https://github.com/odegeasslbc/FastGAN-pytorch>

entailing several heuristics for different hyperparameters. We find the automatic option very robust for both architecture and most hyperparameters. The exception is the R1 gradient penalty [50], which is highly dependent on the dataset. For all large datasets, the Gansformer codebase suggests suitable values for StyleGAN2. For the small datasets at 256^2 and 1024^2 , we perform a grid search over $\gamma \in \{1, 10, 20, 50\}$. We first train for 1 M *Imgs*, then continue training only the best one. For all AFHQ datasets, we use the same setting as [32]. All experiments employ adaptive discriminator augmentation with the default target value of 0.6.

FastGAN. We replicate the generator and discriminator architecture of the official FastGAN codebase. FastGAN is robust to most hyperparameters; we always use a learning rate of 0.0002 and train with a hinge loss. The only sensitive hyperparameter with direct impact on performance is the batch size. Interestingly, FastGAN profits of smaller batch sizes. The default suggested by [49] is a batch size of 8. We conduct a search over 8, 16, 32, and 64, a batch size of 16 further improves the results, while larger batch sizes decrease performance and even result in divergence in some cases. We employ differentiable augmentation [89] of color, translation, and cutout.

Projected GAN. We use the same architecture, learning rate (0.0002), batch size (64), and hinge loss for all experiments at all resolutions. Compared to FastGAN, we see a slight improvement when increasing model capacity; we double the channel count in each dimension, from a base value of 64 to 128. The multipliers for the base value are as follows (resolution: multiplier): $4^2 : 16, 8^2 : 8, 16^2 : 4, 32^2 : 2, 64^2 : 1, 128^2 : 0.5, 256^2 : 0.25, 512^2 : 0.125$. We did not observe similar improvements for FastGAN when increasing capacity. We employ differentiable augmentation [89] of color, translation, and cutout. Lastly, to extract feature maps of intermediate layers of the feature networks, both CNNs and visual transformers, we follow the protocol presented in the MiDAS [62] codebase⁸. For all EfficientNets and ResNets, we use features at spatial resolutions $r = \{64^2, 32^2, 16^2, 8^2\}$, for DeiT and ViT, we use layers $l = \{3, 6, 9, 12\}$. The CSM blocks follow a residual design typically used in architectures for dense prediction [62]. The lower-resolution feature is passed through a residual 3×3 convolution block; the higher-resolution feature is added, followed by a second residual block and bilinear upsampling, followed by a 1×1 convolution.

The discriminator architectures are shown in Table 11 where n_i are the channels of the different feature network stages, c_{in} and c_{out} are the input and output channels of the DownBlock *DB*. A DownBlock consists of a convolution with k size $k = 4$ and stride $s = 2$, BatchNorm, and LeakyReLU with a slope of 0.2. We apply spectral normalization on all convolution layers *Conv*.

Discriminator L_1	Discriminator L_2	Discriminator L_3	Discriminator L_4
$DB(c_{in} = c_1, c_{out} = 64)$	$DB(c_{in} = c_2, c_{out} = 128)$	$DB(c_{in} = c_3, c_{out} = 256)$	$DB(c_{in} = c_4, c_{out} = 512)$
$DB(c_{in} = 64, c_{out} = 128)$	$DB(c_{in} = 128, c_{out} = 256)$	$DB(c_{in} = 256, c_{out} = 512)$	$Conv(c_{in} = 512, c_{out} = 1, k = 4)$
$DB(c_{in} = 128, c_{out} = 256)$	$DB(c_{in} = 256, c_{out} = 512)$	$Conv(c_{in} = 512, c_{out} = 1, k = 4)$	
$DB(c_{in} = 256, c_{out} = 512)$	$Conv(c_{in} = 512, c_{out} = 1, k = 4)$		
$Conv(c_{in} = 512, c_{out} = 1, k = 4)$			

Table 11: Discriminator Architectures.

⁸<https://github.com/intel-isl/MiDaS>